ATOMIC SCALE STRUCTURE VARIATIONS AT FERROELECTRIC DOMAIN WALLS IN MULTIFERROIC $BIFEO_3$

LEUNG MAN HO

MPhil

The Hong Kong Polytechnic University

2019

The Hong Kong Polytechnic University

Department of Applied Physics

Atomic Scale Structure Variations at Ferroelectric Domain Walls in Multiferroic $BiFeO_3$

LEUNG MAN HO

A thesis submitted in partial fulfillment of the requirements

for the degree of Master of Philosophy

August, 2018

CERTIFICATE OF ORIGINALITY

I hereby declare that this thesis is my own work and that, to the best of my knowledge and belief, it reproduces no material previously published or written, nor material that has been accepted for the award of any other degree or diploma, except where due acknowledgement has been made in the text.

_____ (Signed)

_____LEUNG MAN HO_____ (Name of student)

Abstract

Ferroelectric materials have been intensively explored because of their attractive future in electronic industries. Among all kinds of ferroelectric materials, a considerable amount of researches have been conducted on the applications and the natures of $BiFeO_3$ owing to its improved ferroelectric properties. It has been demonstrated that the electrical properties of the ferroelectric domain walls such as the electrical conductivity can be different from that of the bulk ferroelectric domains. Recently, 109° ferroelectric domain walls have been widely examined but inadequate attention has been paid to the promising future of the 180° ferroelectric domain walls. It has been stated that ferroelectric 180° domain walls may contribute to the polarization response and possess enhanced electrical properties. Therefore, the study on 180° ferroelectric domain walls is critical. However, the detailed atomic structure at the ferroelectric 180° domain walls has not been fully established. Recent studies have focused on the polarization configurations near the domain walls without clarifying the detailed atomic structure.

In this work, we examined the atomic scale structure and the polarization configurations using the aberration-corrected scanning transmission electron

microscopy *Z*-contrast imaging with sub-Ångstrom resolution. Results implied that 45° inclined ferroelectric 180° domain walls were obtained above the $SrRuO_3$ bottom electrode instead of the 71° and 109° domain walls which may be due to the effect of $BiFeO_3$ thin film thickness. Besides, the customized Matlab image analysis demonstrated that the lattice parameters depend on the polarization configurations. The observed variations in lattice parameters across the domain walls are attributed to the displacement of the Bi cations induced by the ferroelectric spontaneous polarization. It is also demonstrated that the orientation of the ferroelectric 180° domain walls will be affected by the monoclinic distortion of the substrate. More importantly, substrate interface terminations also play a critical role on the formation of 180° domain walls by switching the sign of the built-in electric field at the interface. Considering the polarization discontinuity model at the heterostructure interface, the polarization configurations of the domains will be strongly influenced by the terminating layer of the substrate. Specifically, spatially varying the interfacial atomic termination can produce both positive and negative built-in electric fields along the interface, and the boundaries across which the built-in field switches sign favor the formation of 180° domain walls in ferroelectric $BiFeO_3$. This indicates an effective strategy using precisely patterned heterostructure to 'plant' ferroelectric

domain walls at the designated sites and to make artificial domain structure with desirable polarization configuration, as demonstrated by theoretical calculations.

This work provided the preliminary understanding about the relationship between polarization configuration and atomic scale structure at $BiFeO_3$ ferroelectric 180° domain walls and filled the knowledge gap in the field of ferroelectric materials and pointed the way to optimize the multiferroic properties of $BiFeO_3$. Finally, the demonstrated polarization configuration and atomic structure mapping approach can be applied to other ferroelectric materials, to explore the promising correlation between atomic structure and ferroelectric property. Therefore, it could provide critical insights into the application of ferroelectric materials in different electronic devices.

THE HONG KONG POLYTECHNIC UNIVERSITY

Presentation in international conferences

1. Man Ho LEUNG and Ye ZHU, “Atomic scale structure variations at ferroelectric domain walls in multiferroic $BiFeO_3$,” European Materials Research Society 2018 Spring meeting, Strasbourg, France, 18th June 2018.

Acknowledgements

I would like to express my sincere appreciation to my supervisor Dr. Y. Zhu and Prof. J. Y. Dai for their fantastic guidance, constant support and frequent motivation throughout my whole period of research study.

Besides, I would also thank Prof. Ramesh's group for providing the $BiFeO_3$ materials, Dr. Z. Liu and his team for the excellent collaborations and expert advices. I would also like to thank my research colleagues for their technical support, advices and encouragement.

Finally, I would to thank the departmental and all the technical staff for their unselfish helps. I also appreciate the support from my department and the technical support from the Materials Research Centre of the Hong Kong Polytechnic University.

THE HONG KONG POLYTECHNIC UNIVERSITY

Table of contents

List of figures and table

Chapter 1 Introduction

1.1 Perovskite oxides

Metal oxides have been widely studied due to their attractive physical and chemical properties for both fundamental researches and potential applications. Oxides comprised by two or more cations are classified as complex oxides while oxides with different oxidation states for single cation are considered as mixed oxides [1]. The most commonly investigated complex oxides are the spinel and perovskite oxides. Spinel group is defined as the metal oxides with AB_2X_4, where A and B represent metal cations while X represents chalcogenide anions such as oxygen and sulphur [1, 2]. The conductivity of spinel oxides depends on the degree of cations disorder. Therefore, spinel oxides exhibit a variety of physical properties with different structures which provides a considerable potential for applications. However, among all kinds of metal oxides, perovskite oxides show a widest diversity of properties.

Perovskite oxides have a chemical formula of ABO_3 which consist of 12 coordinated A site cations at the corners of the unit cell, 6 coordinated B site cations at the center of the unit cell and face centered octahedral oxygen anions [3, 4]. The A site cations are generally the rare earth elements or alkaline earth metals while B sites cations

are usually the *d*-block transition metals. Perovskite oxides are ideally in cubic structure and the schematic diagram of a typical perovskite oxides structure is shown in Figure. 1.1. However, different degrees of symmetric distortions would occur in some perovskite oxides which will become various structural variants such as the orthorhombic and rhombohedral structures [4-6]. In order to fully understand the structural variations of perovskite oxides, the stability of the structure can be ascertained by the tolerance factor *t* [3]. For an ideal perovskite cubic unit cell, the relationship applies:

$$r_A + r_O = \sqrt{2}\,(r_B + r_O)$$

where r_A, r_B and r_O are the ionic radius of A site cations, B site cations and oxygen anions respectively. In addition, the tolerance factor should be taken into consideration for structural distortions and the relationship among the ionic radii becomes:

$$r_A + r_O = t\sqrt{2}\,(r_B + r_O)$$

According to Goldschmidt tolerance factor, an ideal cubic structure can be established when *t* is in the range of 0.9 to 1. For the range of $0.7 < t < 0.9$, the perovskite oxides could have orthorhombic or rhombohedral structures and for $t > 1$, the structure becomes hexagonal [7]. Generally, the value of *t* is determined by oxygen octahedral tilting,

octahedral distortion and cations displacement. It can also be seen that the ionic size of the cations will lead to different tolerance factors and hence different structures. The changes of perovskite structure induced by different ionic sizes of cations [1] are shown in Figure 1.2.

Moreover, substitution of A site or B site cations by dopants will also result in the distortion of perovskite oxides. It has been reported that dopants with different ionic sizes than A or B site cations will permute the structures of the perovskite oxides and therefore prompt diverse physical properties [8-9].

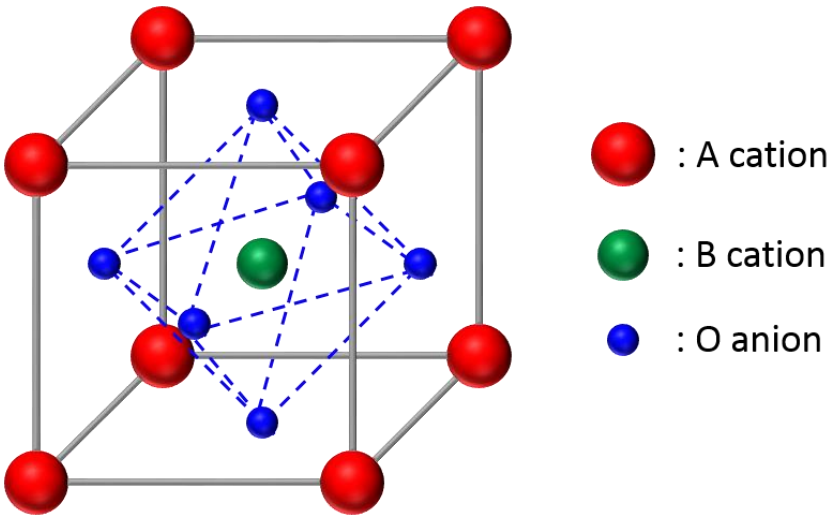

Figure 1.1 ABO_3 perovskite oxides cubic unit cell.

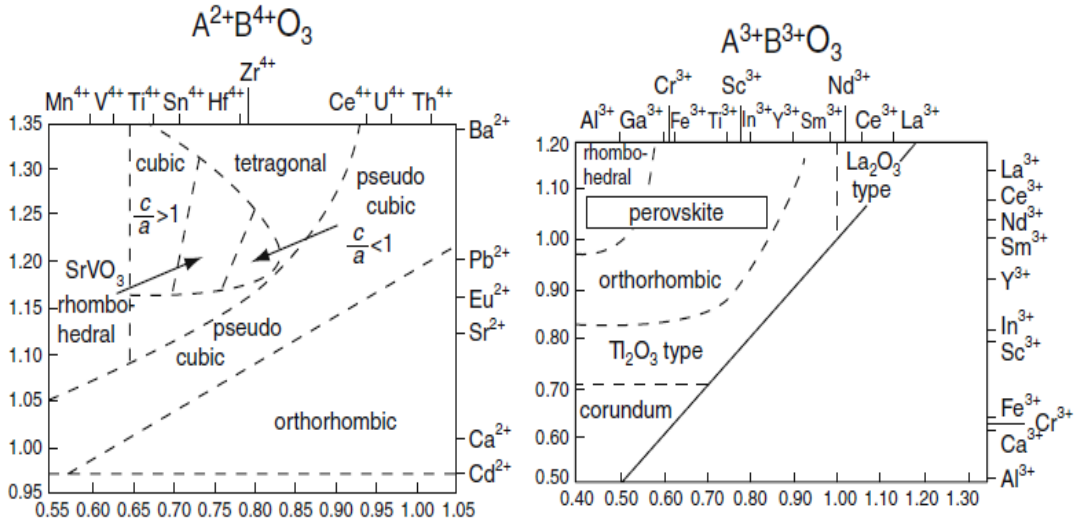

Figure 1.2 The changes of perovskite structure induced by different ionic sizes of cations [1].

1.2 Multiferroic materials

Perovskite oxides with different structures possess a wide variety of physical properties such as piezoelectricity, electrical conductivity, ion conductivity, ferroelectricity and ferroelasticity [6, 10-11]. Ferroic properties including ferroelectricity, ferroelasticity and ferromagnetism were extensively studied and applied in electronic industries. Ferroic materials acquiring two or more ferroic properties simultaneously are classified as multiferroic materials [6]. Apart from the intriguing independent ferroic properties, the coupling between the properties is also fascinating for various applications. The relationship among all kinds of properties is shown in Figure 1.3.

Multiferroic materials have attracted much attention due to their ferroelectricity, ferromagnetism, ferroelasticity and the magnetoelectric coupling. Next, the mentioned properties will be briefly discussed.

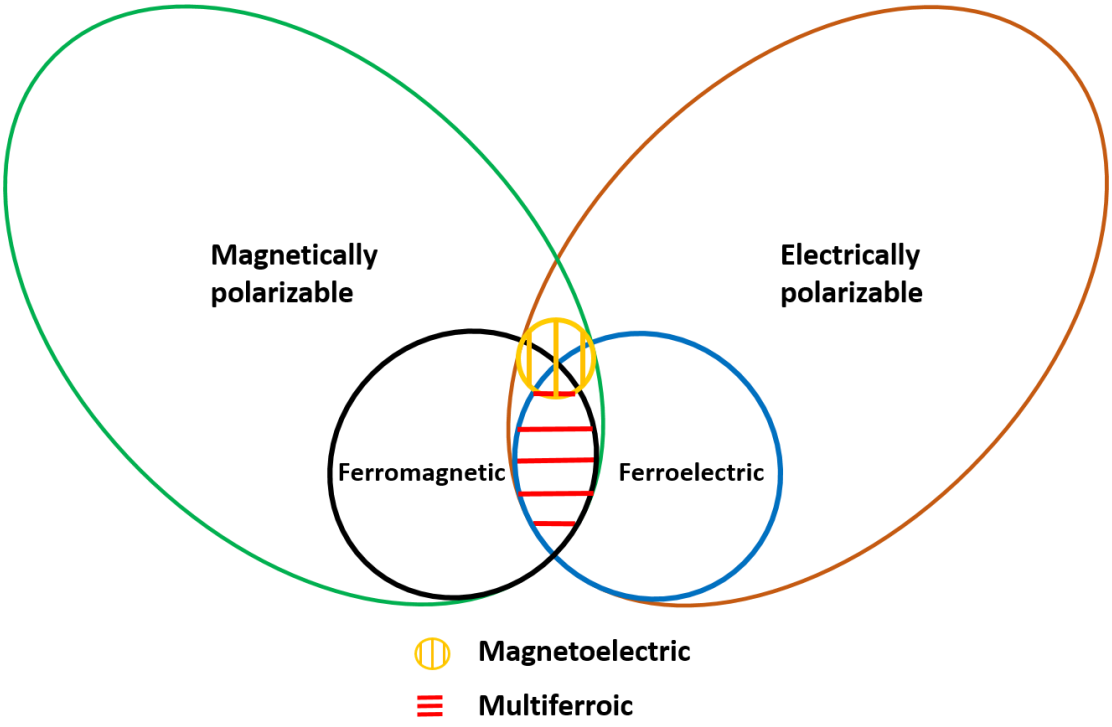

Figure 1.3 Relationship and coupling among different ferroic properties.

1.2.1 Ferroelectricity

Recently, tremendous attention has been drawn on ferroelectric materials because of their promising application in numerous electronic devices, for instance, capacitors, non volatile memory devices and thermistors [12]. Ferroelectricity is defined as the dielectric materials that exhibit a spontaneous polarization and the polarization direction can be

reversed by applying an external electric field [12]. The nature of the spontaneous polarization of the ferroelectric materials is restricted by the Curie temperature (T_c) which is the transition temperature between ferroelectric and paraelectric states. For temperature above T_c, the materials become paraelectric and the spontaneous polarization will vanish. For temperature below T_c, they become ferroelectric and the spontaneous polarization depends on the applied electric field. The behavior of the spontaneoues polarization is characterized as a hysteresis loop and is reversible by applying different electric fields [13]. In the hysteresis loop, the spontaneous polarization without applied electric field is denoted as remnant polarization P_r. The dependence of spontaneous polarization on applied electric field is presented as Figure 1.4. Considering traditional tetragonal perovskite ABO_3 structure such as $BaTiO_3$ and $PbZr_xTi_{1-x}O_3$ (PZT), a shifting of the centered B site cations will be induced relative to the oxygen octahedra by the applied external electric field. The shifting of the centered B site cations and the oxygen octahedra are in different degrees, such that the displacement of oxygen octahedra is larger than that of the centered B site cations, and hence the loss of symmetry from cubic to tetraganol unit cells [14-18]. As a spontaneous polarization vector should be from the negative charge to positive charge, the larger displacement of oxygen octahedra will lead to an electric dipole pointing to the B site cations. Therefore, this results in a polarization

opposite to the displacements of B site cations and oxygen octahedra relative to the centre of the unit cell. The schematic diagram of the paraelectric phase of the perovskite ABO_3 structure is shown in Figure 1.5a). The ferroelectric downward polarization with upward displacement of the centered B site cation and oxygen octahera is demonstrated in Figure 1.5b) and the (010) plane of the unit cell is shown in Figure 1.5c).

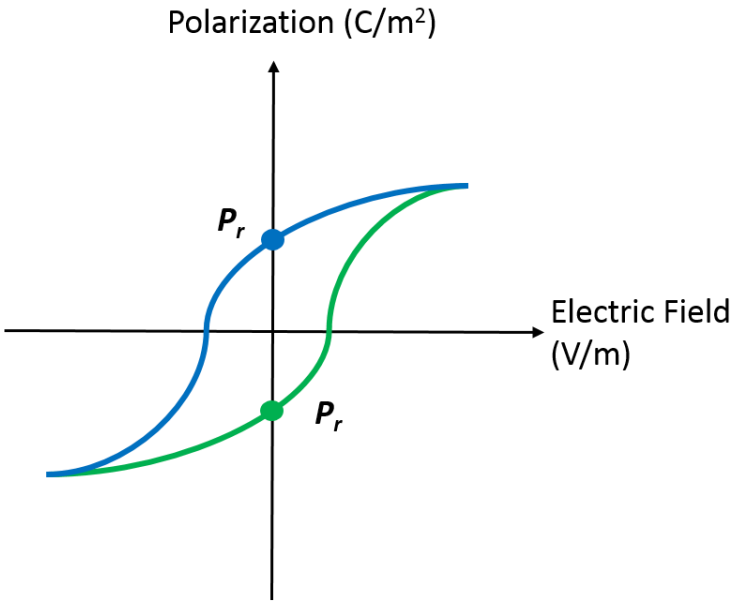

Figure 1.4 Hysteresis loop of spontaneous polarization against applied electric field.

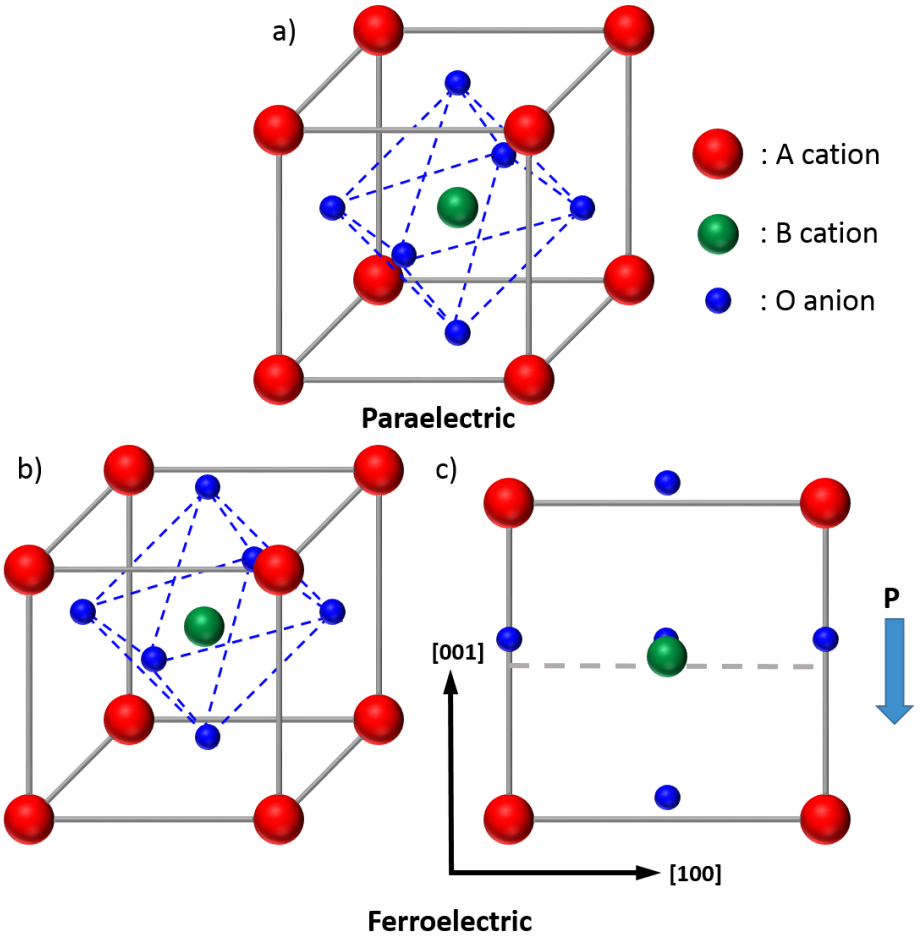

Figure 1.5 Schematic diagram of a) the ferroelectric downward polarization with upward displacement of centered B site cation and oxygen octahedra and b) (010) plane of the polarized unit cell.

For the rhombohedral pseudocubic perovskite unit cell such as $BiFeO_3$, the displacement of the centered B site cations is along one of the body diagonals together with the tilting of the oxygen octahedra. The electric dipole moments or known as the polarization vectors will point from the oxygen octahedra and B site cations to the centres of the unit cells. As the B site cations and the oxygen otaheda are shifted relative to the

position of A site cations, therefore, the polarization direction can be denoted by the direction opposite to the displacement of B site cations or along the displacement direction of A site cations relative to the centered B site cations [19]. The illustrated diagrams of the atomic distortions of the ferroelectric pseudocubic pervoskite unit cell are shown in Figure 1.6a) and b).

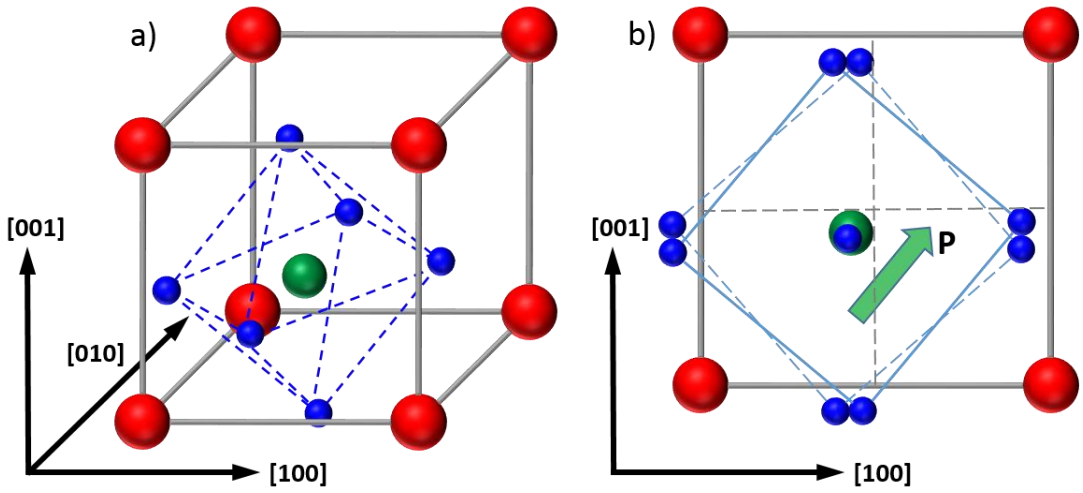

Figure 1.6 Schematic diagram of a) ferroelectric $BiFeO_3$ pervoskite unit cell with [111] polarizaiton vector and b) (010) plane of the unit cell.

1.2.2 Ferromagnetism and Antiferromagnetism

Ferromagnetism refers to the materials that possess stable spontaneous magnetization and can be hysteretically controlled by the external magnetic field.

Similar to ferroelectricity, the spontaneous magnetization without the applied magnetic field is called remnant magnetization B_r.

The alignment of the magnetic moments is crucial to determine the magnetic behavior of the perovskite oxides. In the case when all the magnetic moments are aligned in the same direction, it is ferromagnetic. However, if the magnetic moments are aligned in alternating opposite directions, it is classified as antiferromagnetic [6, 20]. For antiferromagnetism, there is no net magnetic moment as the neighboring spins cancel out each other. Typically, there are three different types of antiferromagnetism which are the A, C and G type antiferromagnetism. In A type, the magnetic moment in the intra planes are in the same direction while in the inter planes are in opposite direction. For C type, the intra plane is antiferromagnetic but the ferromagnetic plane is along the (110) plane [21]. For G type, the magnetic moments are mutually opposite to each neighboring spins [22]. In order words, it is antiferromagnetic in both inter plane and intra plane. The schematic diagram of A, C and G type antiferromagnetism are shown in Figure 1.7.

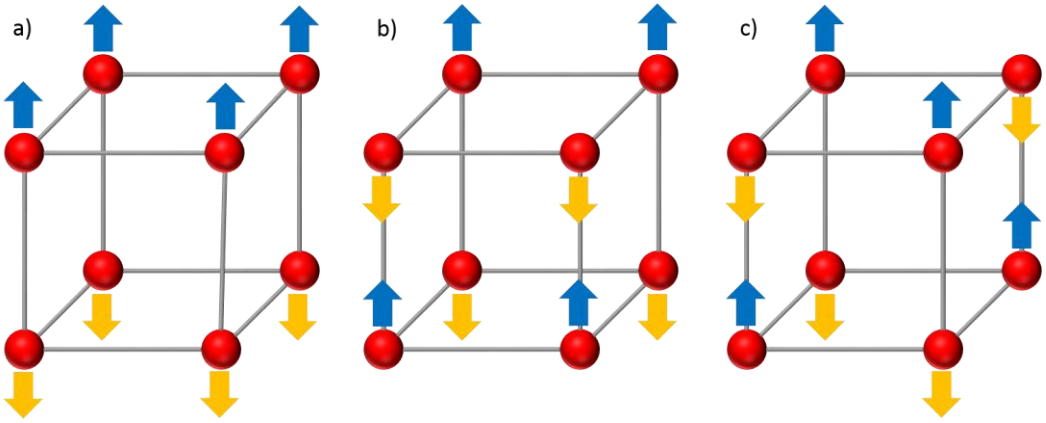

Figure 1.7 Schematic diagram of A, C and G type antiferromagnetism.

1.2.3 Ferroelasticity

Ferroelastic is defined as the second order spontaneous tensor strain induced by the applied stress. The spontaneous tensor strain can also be hysteretically switched by the mechanical stress and it is known as the ferroelastic switching process [6].

Several ferroelastic domains with different orientations can be formed and different ferroelastic states can coexist in the same perovskite oxide crystal since they have the same elastic energy [23]. In multi-domains systems, ferroelastic domain walls are the boundaries formed between two different ferroelastic domains. The existence of ferroelastic domain walls is restricted by the strain compatibility which essentially minimize the strain energy [24-25]. The mechanical deformation of two neighboring domains in parallel to the domain walls should be identical and this will be discussed

later. The domain walls are denoted by the angle difference between two adjacent domains, such as 71°, 90°, 109° and 180° domain walls. Generally, the inversion symmetry of the ferroelastic materials should not be broken by the spontaneous strain [6, 26]. Therefore, considering pure ferroelastic materials, 180° domain walls cannot be formed. Moreover, the 90° domain wall is the most common twin wall in the tetragonal ferroelastic materials and the domain wall is oriented in 45° with respect to the {001} plane [14]. The detailed strain compatibility and the restriction of forming domain walls will be discussed in the later part.

1.2.4 Magnetoelectric coupling

Magnetoelectric coupling is described as the coupling between polarization and magnetization of the materials [6]. The magnetoelectric effect can be described by the Landau-Theory of free energy F in terms of applied electric field E and magnetic field H [27-30]. The expansion of the free energy F is written as:

$$F(E,H) = F_o - P_i^s E_i - M_i^s H_i - \frac{1}{2}\varepsilon_o \varepsilon_{ij} E_i E_j - \frac{1}{2}\mu_o \mu_{ij} H_i H_j - \alpha_{ij} E_i H_j - \frac{1}{2}\beta_{ijk} E_i H_j H_k + \frac{1}{2}\gamma_{ijk} H_i E_j E_k + \cdots$$

where i, j, k are the spatial indices, F_o is the free energy without the electromagnetism, P^s and M^s denote the spontaneous polarization and spontaneous magnetization, ε_o is

the permittivity of free space while ε_{ij} is the second order tensor permittivity, μ_o is the permeability of free space and μ_{ij} is the relative permeability, α_{ij} is the magnetoelectric coupling coefficient, β_{ijk} and γ_{ijk} represent the higher order coefficients.

By differentiating the F against E and H, the polarization and magnetization with coupling effect can be obtained as shown below:

Polarization:

$$P_i(E,H) = -\frac{\partial F}{\partial E_i} = P_i^s + \varepsilon_o \varepsilon_{ij} E_j + \alpha_{ij} H_j + \frac{1}{2}\beta_{ijk} H_j H_k + \cdots$$

and Magnetization:

$$M_i(E,H) = -\frac{\partial F}{\partial H_i} = M_i^s + \mu_o \mu_{ij} H_j + \alpha_{ij} E_j + \frac{1}{2}\gamma_{ijk} E_j E_k + \cdots$$

The magnetoelectric coefficient α_{ij} describes the effects of magnetic field on polarization and electric field on magnetization. It is restricted by the relationship of:

$$\alpha_{ij}^2 \leq \varepsilon_o \varepsilon_{ij} \mu_o \mu_{ij}$$

As ferromagnetic and ferroelectric materials have large permeability and permittivity respectively, therefore, multiferroic materials that possess both ferromagnetism and ferroelectricity are expected to obtain large magnetoelectric coupling effect.

1.3 Geometric orientations of ferroelastic domain walls

In rhombohedral perovskite oxides structure, the structural distortions are along the four body diagonals in the <111> directions of the pseudo-cubic structure with the ferroelectric polarization vectors in the same diagonals which may lead to the formation of eight polarization variants. However, although there are eight polarization variants, they can be considered as four different ferroelastic domain variants with respect to the pseudo-cubic structure. This is the result of identical mechanical strains of positive and negative polarizations. The ferroelastic domains with structural distortions along the four <111> body diagonals are shown in Figure 1.8 with the notations of r_1, r_2, r_3 and r_4. The positive polarizations are denoted by $+P_1$, $+P_2$, $+P_3$ and $+P_4$ while the negative polarizations are denoted by $-P_1$, $-P_2$, $-P_3$ and $-P_4$. Neglecting the polarization, the spontaneous rhombohedral structural distortions induced by the variants r_1, r_2, r_3 and r_4 are assumed to be along the $[\bar{1}11]$, $[111]$, $[\bar{1}\bar{1}1]$ and $[1\bar{1}1]$ directions respectively. Different geometries of domain walls will be formed by two neighboring ferroelastic domains which are the vertically oriented and 45° inclined domain walls. Streiffer et al. [25] reported that the orientations of ferroelastic domain walls should be mechanically compatible that the parallel components of the structure deformation in the two adjacent ferroelastic domains with

respect to the domain wall should be in the opposite directions. This can ensure a zero shear strain on the domain wall produced by the two adjacent domains.

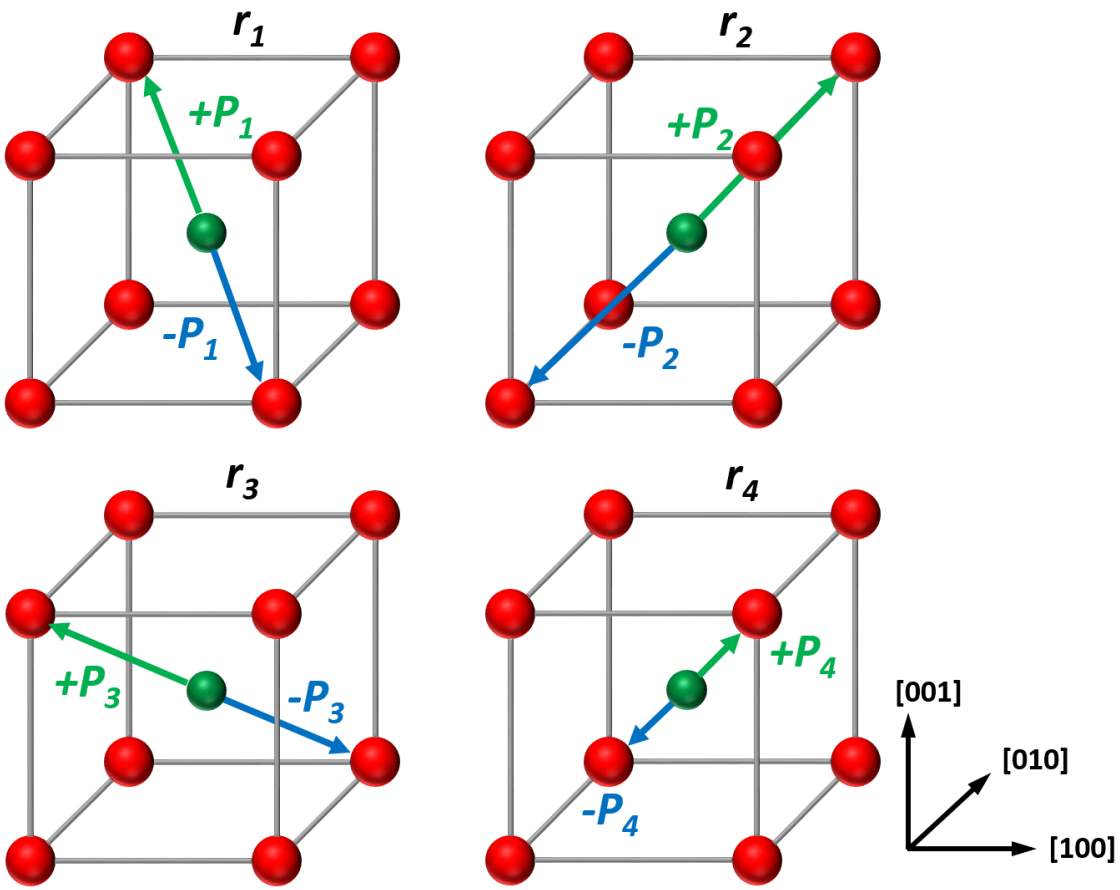

Figure 1.8 Rhombohedral ferroelastic domain variants of r_1, r_2, r_3 and r_4 with four body diagonal distortions. Green arrows represent the positive polarizations $+P_1$, $+P_2$, $+P_3$ and $+P_4$. Blue arrows represent the negative polarizations $-P_1$, $-P_2$, $-P_3$ and $-P_4$.

1.3.1 Vertically oriented ferroelastic domain walls

It is believed that the two antiparallel structural distortion directions of each domain variant can be regarded as identical in ferroelastic domains. For example, $[\bar{1}11]$ and $[1\bar{1}\bar{1}]$ distortion directions are the same for domain variant r_1, while $[111]$ and $[\bar{1}\bar{1}\bar{1}]$ are the same for domain variant r_2. Considering the domain variant r_1 with $[1\bar{1}\bar{1}]$ distortion and r_2 with $[111]$ distortion, the parallel components of the distortions with respect to the (100) domain wall are in the opposite directions and hence it is mechanically compatible. The formation of the (100) domain wall by the domain variants r_1 and r_2 is shown in Figure 1.9. The domains are in a periodically 'puckered' pattern with (001) domain walls in between two different domains and the shearing angle with respect to the substrate is represented by ω_s. Taking variants r_2 and r_4 as another example, the parallel components with respect to (010) plane are along the $[101]$ and $[\bar{1}0\bar{1}]$ directions which are in the opposite directions. Therefore, the (010) domain wall is also mechanically compatible for domain variants r_2 and r_4. Remarkably, for a (001) oriented film, the domain wall along (001) plane would not be obtained as there is no relief of strain energy. Hence, the (001) domain wall is not considered in the vertical {100} plane family.

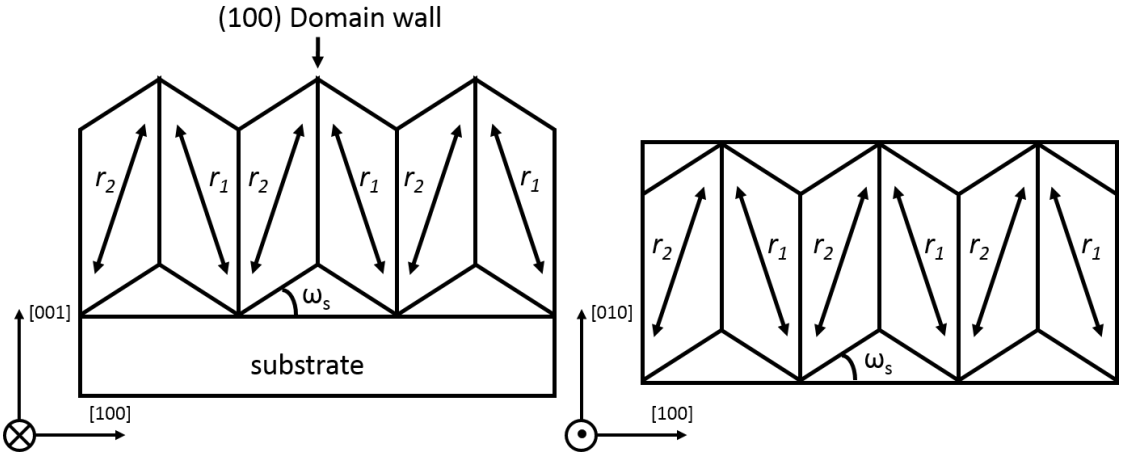

Figure 1.9 Schematic diagram of the domain pattern formed by variants r_1 and r_2 with the (100) domain wall. The shear angle is denoted by ω_s.

1.3.2 45° inclined ferroelastic domain walls

Using the same theory, 45° inclined {101} ferroelastic domain walls can also be formed. For variants r_2 and r_4, the parallel components with respect to (101) plane are along the $[010]$ and $[0\bar{1}0]$ directions. As they are in opposite directions, the (101) domain wall can be obtained. However, as the (110) and $(\bar{1}10)$ domain walls are vertical on the (001) oriented substrate, therefore, they will be excluded in the discussion of 45° inclined {101} ferroelastic domain walls. From Figure 1.10, the (101) ferroelastic domain wall is 45° inclined on the (001) oriented substrate and the shear distortion of the domains is along the $[010]$ direction with the shear angle ω_s.

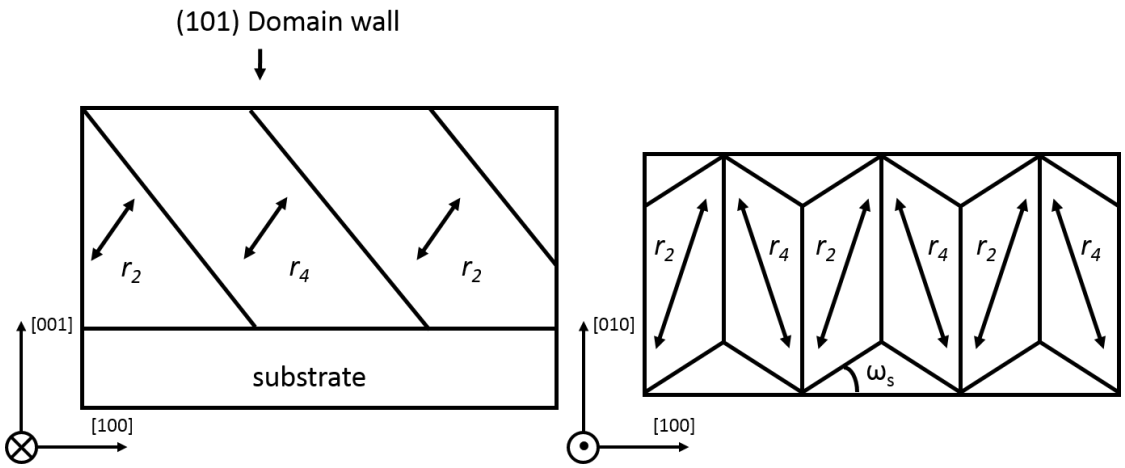

Figure 1.10 Schematic diagram of the domain pattern formed by variants r_2 and r_4 with the 45° inclined (101) domain wall. The shear angle is denoted by ω_s.

To conclude, examining all combinations of two adjacent ferroelastic domains formed by the four variants, the allowed ferroelastic domain walls are shown in Table 1.1.

Table 1. 1 Possible ferroelastic domain walls formed by different structural variants. The asterisk represents the unexpected domain walls.

Variant	1	2	3	4
1		(100)	(010)	(001)*
		(011)	$(\bar{1}01)$	$(\bar{1}10)$*
2			(001)*	(010)
			(110)*	(101)
3				(100)
				$(0\bar{1}1)$

1.4 Geometric orientations of ferroelectric domain walls

In ferroelectric materials, surface charges will be induced by the spontaneous polarization. The surface charges will result in the depolarization field if they are unscreened. Compensation of surface charges can be achieved by adding conducting electrodes which can provide free carries [31-35]. Moreover, ferroelectric domains with oppositely oriented polarization and zero net polarization can cancel out the surface charges. The formation of ferroelectric domains can release the total elastic and electrostatics energy of the materials by the energy expense of forming the ferroelectric domain walls [24, 36].

Ferroelectric domains are defined as the regions in which spontaneous polarizations are oriented in the same direction. In bulk ferroelectric materials, different orientations of ferroelectric domains can be formed under the mechanical and electrical compatibility [25]. For the adjacent domains with different polarization directions, a domain wall will be formed in between the domains and categorized by the angle difference between the domains [37].

The formation and the orientation of the ferroelectric domain walls in rhombohedral perovskite oxides are limited by the mechanical and electrical compatibility. The above discussed ferroelastic domain walls are only mechanically

compatible without considering the electrical compatibility. However, spontaneous polarization should also be examined for ferroelectric domain walls in order to maintain the electrical compatibility. Streiffer et al. [25] demonstrated that there are two limitations on the formation of charge neutral ferroelectric domain walls. Firstly, the mechanical deformation prompted by the two adjacent domains in parallel to the domain walls should be in the opposite distortion directions in order to maintain the mechanical compatibility. Secondly, as to fulfill the electrical compatibility, the normal components of spontaneous polarization of the two adjacent domains across the domain wall should be conserved which means they should be in the same direction or with zero normal component.

For each structural variant, there are two polarization vectors which are in the opposite directions. For example, domain variant r_3 has the polarization vectors along $[\bar{1}\bar{1}1]$ and $[11\bar{1}]$ directions and they are represented by $+P_3$ and $-P_3$. Evaluating domain variant r_3 with $-P_3$ $[11\bar{1}]$ polarization and r_4 with $+P_4$ $[1\bar{1}1]$ polarization, the normal components of the spontaneous polarization across the (100) domain wall are both in $[100]$ direction. Therefore, a charge neutral domain wall can be achieved and the schematic diagram of the vertical ferroelectric (100) domain wall formed by the polarization variants $-P_3$ and $+P_4$ is shown in Figure 1.11. Similarly, 45° inclined

ferroelectric domain walls can also be obtained by using the same theory and all possible charge neutral vertical {100} and 45° inclined {101} ferroelectric domain walls formed by different polarization variants are shown in Table 1.2.

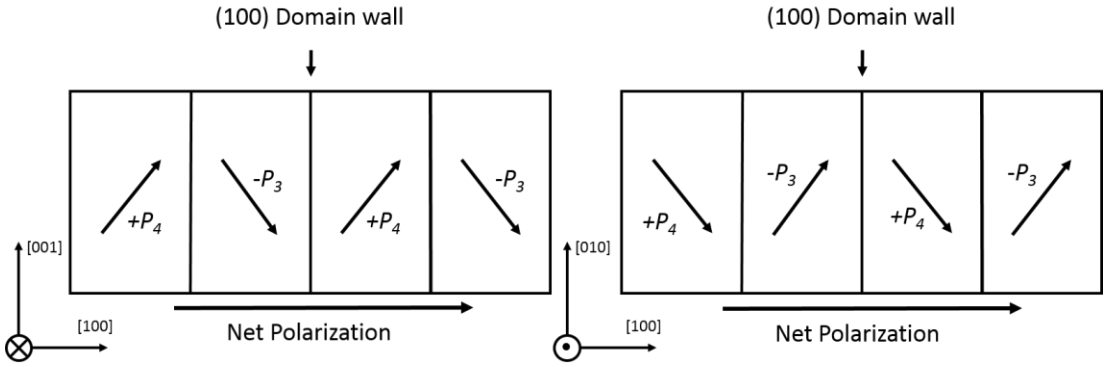

Figure 1.11 Schematic diagram of the (100) ferroelectric domain wall between $-P_3$ and $+P_4$ polarization variants.

Table 1. 2 Possible ferroelectric domain walls formed by different polarization variants. The asterisk represents the unexpected ferroelectric domain walls. Where *h*, *k* and *l* represent the Miller indices and the summation should be equal to 0.

Variant	$-P_1$	$+P_2$	$-P_2$	$+P_3$	$-P_3$	$+P_4$	$-P_4$
$+P_1$	(*hkl*)	(011)	(100)	$(\bar{1}01)$	(010)	(001)*	$(\bar{1}\bar{1}0)$*
$-P_1$		(100)	(011)	(010)	$(\bar{1}01)$	$(\bar{1}\bar{1}0)$*	(001)*
$+P_2$			(-*hkl*)	(001)*	(110)*	(101)	(010)
$-P_2$				(110)*	(001)*	(010)	(101)
$+P_3$					(-*h*-*kl*)	$(0\bar{1}1)$	(100)
$-P_3$						(100)	$(0\bar{1}1)$
$+P_4$							(*h*-*kl*)

Moreover, in rhombohedral perovskite oxides structure, there are three types of ferroelectric domain walls which are the 71°, 109° and 180° domain walls while the 90° domain wall only occurs in tetragonal and orthorhombic perovskite oxides. The illustration diagram of different types of ferroelectric domain walls is shown in Figure 1.12. The polarization directions are represented by the green arrows. The red, blue and yellow arrows indicate the angle difference of 71°, 109° and 180° between two neighbouring domains respectively. The geometries of the ferroelectric domain walls formed by different ferroelectric domains can also be explained by the mechanical and electrical compatibility.

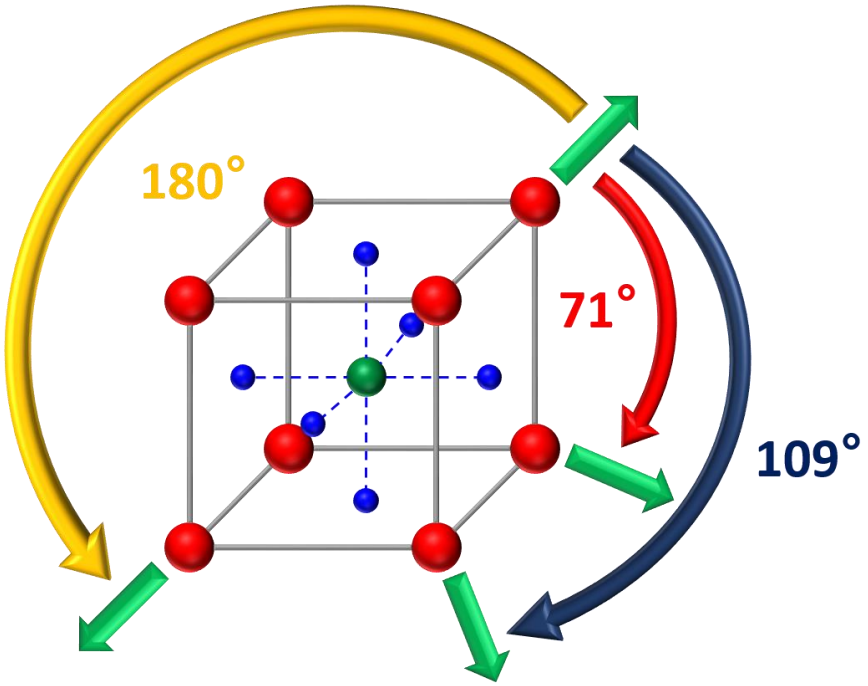

Figure 1.12 Illustration diagram of 71°, 109° and 180° ferroelectric domain walls. Green arrows represent the <111> polarization directions. Red, blue and yellow arrows represent the 71°, 109° and 180° domain configurations respectively.

For all kinds of 71° ferroelectric domain walls, they should be 45° inclined on the (001) oriented substrate due to the mechanical and electrical compatibility. An example of the 45° inclined 71° domain wall formed by $+P_2$ and $+P_4$ polarization variants is demonstrated in Figure 1.13. From Figure 1.13, the parallel components of the polarization variants with respect to the (101) domain wall are antiparallel while the normal components across the domain wall are in the same direction. Hence, the

formation of the charge neutral 71° (101) ferroelectric domain wall is mechanically and electrically compatible.

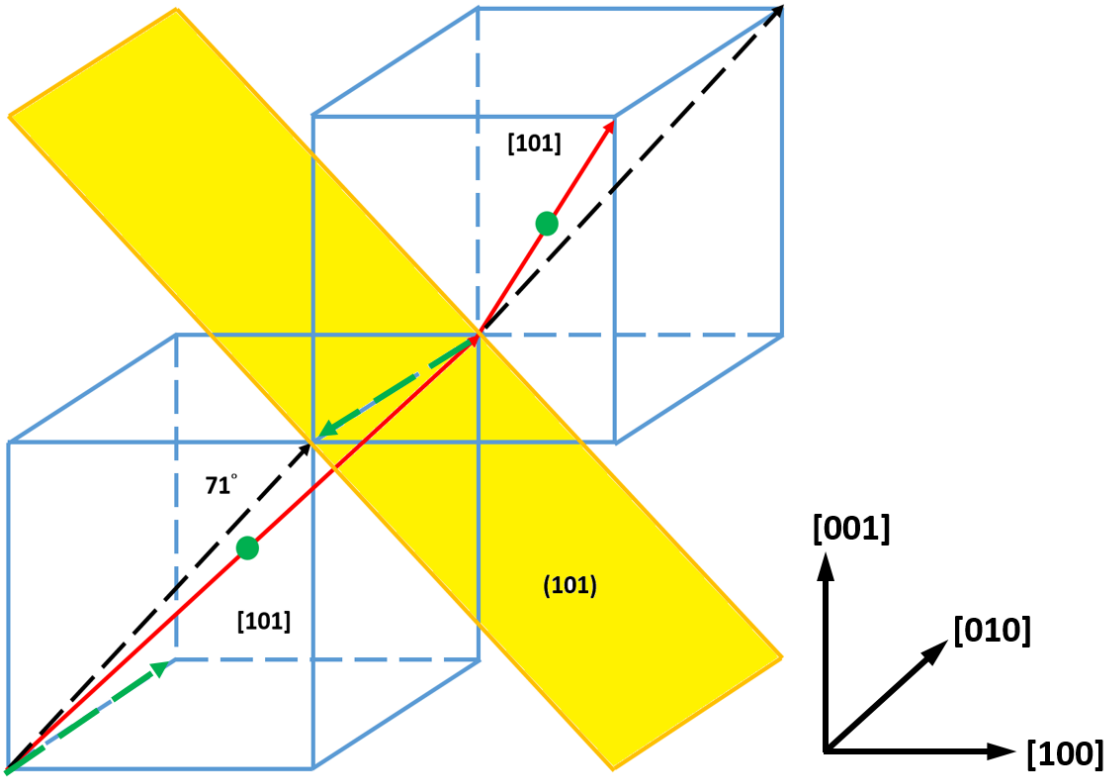

Figure 1.13 Schematic diagram of the 71° ferroelectric domain wall. Red, green dash and black dash arrows represent the polarization variants, parallel components and normal components on the domain wall respectively. The yellow plane demonstrates the inclined 71° ferroelectric domain wall.

For charge neutral 109° ferroelectric domain walls, in order to fulfill the mechanical and electrical compatibility, the domain walls would be in vertical

direction on the (001) substrate. Figure 1.14 shows the 109° (100) ferroelectric domain wall formed by polarization variants $-P_3$ and $+P_4$.

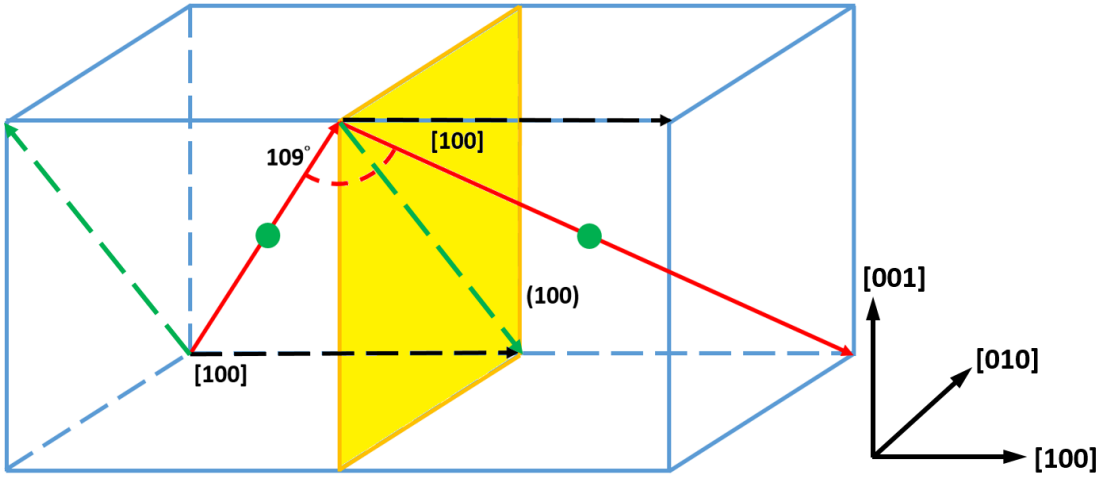

Figure 1.14 Schematic diagram of 109° the domain wall. Red, green dash and black dash arrows represent the polarization variants, parallel components and normal components on the domain wall respectively. The yellow plane demonstrates the vertical 109° domain wall.

According to the same theory, 180° domain walls are also found to be 45° inclined on (001) substrate. As there is no normal component of polarization variants on 180° domain walls, it is electrically compatible. The formation of the 180° domain wall formed by polarization variants $+P_2$ and $-P_2$ is shown in Figure 1.15.

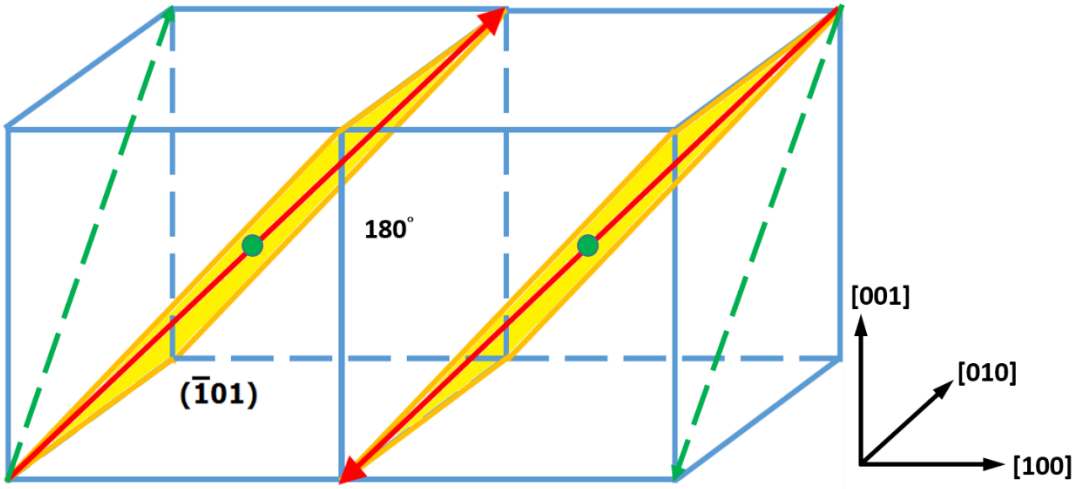

Figure 1.15 Schematic diagram of the 180° domain wall. Red and green dash arrows represent the polarization variants and parallel components on the domain wall respectively. The yellow plane demonstrates the inclined 180° domain wall.

1.5 Bismuth ferrite ($BiFeO_3$)

Among all kinds of ferroelectric materials, there has been growing interest in $BiFeO_3$ due to its promising properties. We had chosen $BiFeO_3$ as a model system for its high ferroelectric Curie temperature (T_c ~1100 K) and large ferroelectric polarization (P_s ~100 μC/cm^2) when comparing with other typical ferroelectric materials such as $BaTiO_3$, PZT and $PbTiO_3$ which are shown in Table 1.3. In addition, it has a relatively lower bandgap energy from 2.6 eV to 3.0 eV which is promising for the application in photovoltaic devices comparing to other wide-bandgap ferroelectric

materials [38-39]. $BiFeO_3$ is classified as a rhombohedral perovskite oxide structure of space group *R3c* with the lattice constant a = 3.965Å, rhombohedral angle α = 89.4° and the tolerance factor t = 0.96 [40]. The polarization of $BiFeO_3$ is along the <111> directions and the rotation of the oxygen octahedral is around 11° to 14° about the polarized <111> axis. The rotation of oxygen octahedral is denoted as $a^-a^-a^-$ by the Glazer's notation and this would lead to the changing of Fe-O-Fe angle to be around 154° to 158° [41]. Moreover, $BiFeO_3$ is an archetype multiferroic material with a strong coupling between ferroelectricity and *G*-type antiferromagnetism (with Néel temperature $T_N \sim$ 650K) at room temperature.

Table 1. 3 Characteristics of different ferroelectric materials.

Materials	Spontaneous polarization	Band gap
$BiFeO_3$	~100 μC/cm²	2.6-3.0eV
$BaTiO_3$	~26 μC/cm²	3.2-3.5eV
PZT	~30 μC/cm²	3.3-3.4eV
$PbTiO_3$	~70 μC/cm²	3.5-3.9eV

There are tremendous interests in $BiFeO_3$ for both fundamental research and technology applications due to its fantastic ferroelectric, optical and magnetic properties as well as the inter-coupling between the properties.

1.6 Motivation of research

Ferroelectricity provides a rich ground to explore both fundamental science and technological applications such as electronics and solar cells. Owing to the promising future of the applications of $BiFeO_3$, a significant amount of research efforts have been conducted to study the natures and the applications of ferroelectric $BiFeO_3$. In order to maintain a sustainable development of ferroelectric materials, apart from exploring the mechanism of the domain structure formation, the analysis of ferroelectric domain walls is also necessary. It has been discovered that the properties of ferroelectric domain walls can be different from the domains including the electrical conductivity and magnetic properties [42-44]. In addition, several studies on the functionalities and the engineering of the ferroelectric domain walls have been conducted. Jan Seidel et al. [42] revealed that the domain walls can be more conductive than that of the bulk domains, a result of bandgap changing and polarization rotation inside domain walls which allow more charge carries to be accumulated in domain walls. Besides, photovoltaic performances at ferroelectric domain walls can also be improved, which are attributed to the separation of charge carries across the domain walls [45].

Despite the importance of ferroelectric domain walls, the detailed atomic structure at the domain walls is far from fully understood. Conventional X-ray diffraction-based structure determination requires periodic structure and is impractical to solve the non-periodic local structure at interfaces such as the domain walls. The domain wall structure has been mostly studied using theoretical calculations due to the lack of experimental characterization approaches. Only recently, the advent of aberration-corrected transmission electron microscopy (TEM) and scanning TEM (STEM) has made it possible to directly resolve the atomic structure at domain walls in real space. Using aberration-corrected STEM, Nelson et al. [35] observed the occurrence of triangular-shaped vortex nanodomains at ferroelectric heterointerfaces. In addition, another research in ferroelectric materials discovered that a tetragonal distortion in charged domain walls is induced by the polarization bound charge of the charged domain walls [46]. On the other hand, these pioneering work mostly focused on the polarization configurations around domain walls, without clarifying the detailed atomic structure around the domain walls.

In recent years, the 109° ferroelectric domain walls have been widely investigated in $BiFeO_3$. However, little attention has been paid to the promising future of 180° ferroelectric domain walls. It has been demonstrated that 180° domain walls possess

enhanced electrical conductivity and contribute to the polarization response [42]. In addition, Fancher et al. [47] discovered that 180° domain wall motion could improve the piezoelectric response of the ferroelectric $BiFeO_3$. It shows that 180° ferroelectric domain walls have the promising value to be studied.

This study will provide the detailed atomic structure at $BiFeO_3$ domain walls and therefore fill the knowledge gap in the field of ferroelectricity. The obtained correlation between polarization and atomic structure variation will significantly advance the understanding of ferroelectric domain structure and point the way to optimize the multiferroic properties of $BiFeO_3$ for future applications. At last, the demonstrated approach can be generalized to other ferroelectric materials, to explore the fascinating interplay between atomic structure and ferroelectric property.

1.7 Scope of work

In this work, there are two main objectives. The first one is by using the state-of-the-art aberration-corrected STEM to study the atomic structure variations and the polarization configurations across the domain walls in $BiFeO_3$ perovskite oxide. The second one is to understand the relationship between the domain wall structure and heterostructure interface.

This thesis is comprised of five chapters. In chapter one, it begins with the fundamental introduction of the perovskite oxides, multiferroic materials with different types of ferroic properties, ferroelectric domains and domain walls, $BiFeO_3$, motivation and the objectives of the work.

In chapter two, it describes various techniques utilized in this work including characterizing the materials using atomic force microscopy and piezoresponse force microscopy, aberration-corrected STEM and atomic scale structure mapping by Matlab program.

In chapter three, it presents the results of atomic structural variations at ferroelectric $BiFeO_3$ domain walls through polarization and lattice parameter mappings.

In chapter four, the effects of interface termination on structural variation of $BiFeO_3$ will be discussed. Moreover, the polarization engineering of the domains will be examined.

In chapter five, there will be the conclusions of the whole work and some suggestions for potential future work.

Chapter 2 Transmission Electron Microscopy and Other Experimental Techniques

2.1 Materials and characterization

The $BiFeO_3$ thin films were grown by the pulsed laser deposition (PLD) technique in Prof. Ramesh's group at the University of California at Berkeley. PLD can be used to deposit high-quality thin films by a wide range of deposition parameters, including high temperature deposition to improve the crystallinity [48-52].

PLD is classified as the physical vapor deposition process which requires a high power pulsed laser beam. The laser beam will be focused on the target materials and the materials will be vaporized to become a plasma. The plasma target materials would then be deposited on the substrates. The vaporization of the target materials is generally called 'ablation' and the ablation is carried on a rotating disc which acts as a support for collecting the ablated materials [53]. In the PLD, the nucleation of the materials is controlled by several factors including substrate temperature, substrate surface, laser parameter and background pressure: Nucleation density of the target materials would be decreased by the increase of

substrate temperature. For the substrate surface, as there are miscuts of the substrates and lattice mismatch between the target materials and the substrates, therefore, the nucleation and growth of the target materials would be affected. In addition, the laser parameters such as laser fluence, ionization degree and the laser energy may alter the stoichiometry, nucleation density and the quality of the ablated materials. Besides, a high oxygen pressure in the deposition chamber would ensure the correct stoichiometry of the materials by preventing oxygen vacancies [54]. In this work, the $BiFeO_3$ is deposited on the $DyScO_3$ (110) substrate with a $SrRuO_3$ (001) conducting layer in between the $BiFeO_3$ and $DyScO_3$. The PLD were carried at 700°C with 100 mTorr of O_2 pressure. The grown $BiFeO_3$ film is then characterized by atomic force microscopy (AFM) and piezoresponse force microscopy (PFM). In order to examine the effect of the $SrRuO_3$ conducting layer on the domain pattern of $BiFeO_3$, a comparing sample without the $SrRuO_3$ layer is also fabricated. The AFM and PFM images will be discussed.

On the other hand, the effect of epitaxial strain, substrate symmetry, substrate miscut angles and the electrical boundary conditions should be considered for selecting the growth substrate of the $BiFeO_3$ thin film. It has been reported that a reduction of ferroelectric domain variants by the growth of conducting $SrRuO_3$

bottom electrode [55]. It is the result of the electrical properties of the $SrRuO_3$ layer which can establish a built-in electric field from the thin film to the $SrRuO_3$ layer and hence lead to a downward polarization from the $BiFeO_3$ thin film to $SrRuO_3$. Therefore, the growth of $SrRuO_3$ on the substrate can maintain the formation of domain variants with only downward polarization. Furthermore, the selection of different substrates would also affect the quality of the $SrRuO_3$ conducting layer and the symmetry of the $BiFeO_3$ thin film. It is demonstrated that the orthorhombic (110) rare earth scandate substrates such as $DyScO_3$, $SmScO_3$ and $GdScO_3$ and high miscut angle $SrTiO_3$ can suppress certain types of domain variants [56-58]. Among these substrates, Johann et al. [55] found that cubic $SrTiO_3$ and $DyScO_3$ can obtain a better $SrRuO_3$ quality than $SmScO_3$ and $GdScO_3$. It is due to the fact that the lattice mismatch between $SmScO_3$/$GdScO_3$ and $SrRuO_3$ is too large which leads to the strain relaxation in $SrRuO_3$ and prohibits the domain variant suppression. In addition, comparing to $DyScO_3$, $SrTiO_3$ has a larger lattice mismatch with $BiFeO_3$ which causes the reduction of rhombohedral symmetry of $BiFeO_3$ [59-61]. Therefore, $DyScO_3$ is used as the growth substrate due to its least lattice mismatch with respect to both $SrRuO_3$ and $BiFeO_3$. The comparison of different substrates' lattice constants are shown in Table 2.1.

Table 2. 1 Lattice constants of different substrates and lattice mismatch with repect to $BiFeO_3$ and $SrRuO_3$.

	Lattice constant (Å)	**Lattice misfit with $BiFeO_3$ (3.96 Å)**	**Lattice misfit with $SrRuO_3$ (3.93 Å)**
$SrTiO_3$	3.91	-1.4%	-0.6%
$DyScO_3$	3.94	-0.3%	+0.5%
$GdScO_3$	3.97	+0.2%	+1.0%
$SmScO_3$	3.99	+0.7%	+1.4%

2.1.1. AFM

AFM is a scanning probe microscopy with high resolution up to Å order and it can be used to examine the surface topography of a sample. The working principle of AFM is to apply a tip on the surface of the sample and measure the interaction between the probe and the sample surface such as van der Waals force, electromagnetic force and capillary force. There are two common types of operation modes in AFM which are the tapping mode and the contact mode [62].

In the tapping mode, the tip of cantilever is vibrated at the resonant frequency. During the scanning process, the tip would be tapping on top of the sample and the disturbance of the oscillation by the sample is recorded. The phase contrast mode

can be simultaneously operated with the tapping mode which provides the surface properties of the sample including friction, adhesion and viscoelasticity.

In the contact mode, the AFM tip will be in contact with the sample and a constant deflection of the cantilever would be obtained by adjusting the height of the tip. The changes in the *z* direction of the signal would provide the detailed topography of the sample. The major advantage of using AFM to probe the sample is that it does not require special treatments which may damage the sample. However, the disadvantages are the incapability for probing soft samples as the probing process may lead to the damage of the sample and the tip is non-reusable due to the destruction of the tip during the imaging.

In this work, the AFM images of $BiFeO_3$ film shown in Figure 2.1a) with $SrRuO_3$ conducting layer, and b) without $SrRuO_3$ conducting layer were taken by Prof Ramesh's group at University of California at Berkeley. For the $BiFeO_3$ film grown with the $SrRuO_3$ conducting layer, the roughness of the surface morphology indicates the formation of $SrRuO_3$ islands, instead of a uniform $SrRuO_3$ layer. It has been demonstrated that the gradually increasing $SrRuO_3$ growth rate will result in the change of growth mode from step flow to island formation [63]. In addition, the circular multi-terraces of the $SrRuO_3$ layer will also lead to the formation of

different $BiFeO_3$ domains. For the $BiFeO_3$ film without the $SrRuO_3$ bottom electrode, the surface morphology is smooth. The effect of the presence of $SrRuO_3$ islands on the ferroelectric domain structures will be investigated in Chapter 3.

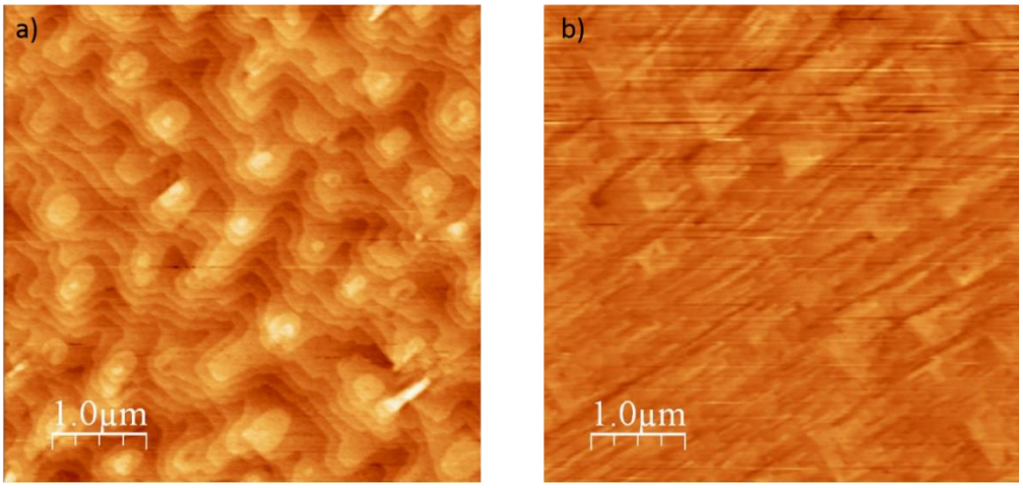

Figure 2.1 AFM images of $BiFeO_3$ film a) with $SrRuO_3$ conducting layer, and b) without $SrRuO_3$ conducting layer.

2.1.1. PFM

PFM is widely applied to study the ferroelectric domains of a material. The technique of PFM is based on a conductive sharp tip. When the tip of PFM is in contact with the ferroelectric or piezoelectric materials, an alternating current (AC) signal is applied to the tip. Due to the converse piezoelectric effect of the materials, there will be mechanical changes and these changes would then induce a deflection

signal of the probe. The signal is then received by a photodiode detector and amplified by a lock in amplifier [64-65]. Therefore, the PFM technique can be used to investigate the ferroelectric domain pattern and the polarization state of the sample. The PFM images of $BiFeO_3$ film with and without $SrRuO_3$ are shown in Figure 2.2. It is evident that there are two types of domains in the $BiFeO_3$ thin film with the $SrRuO_3$ conducting layer while there is only one for the BiFeO3 thin film without $SrRuO_3$. The mechanisms of obtaining different domain walls with the presence and absence of $SrRuO_3$ bottom electrode will also be discussed in Chapter 3.

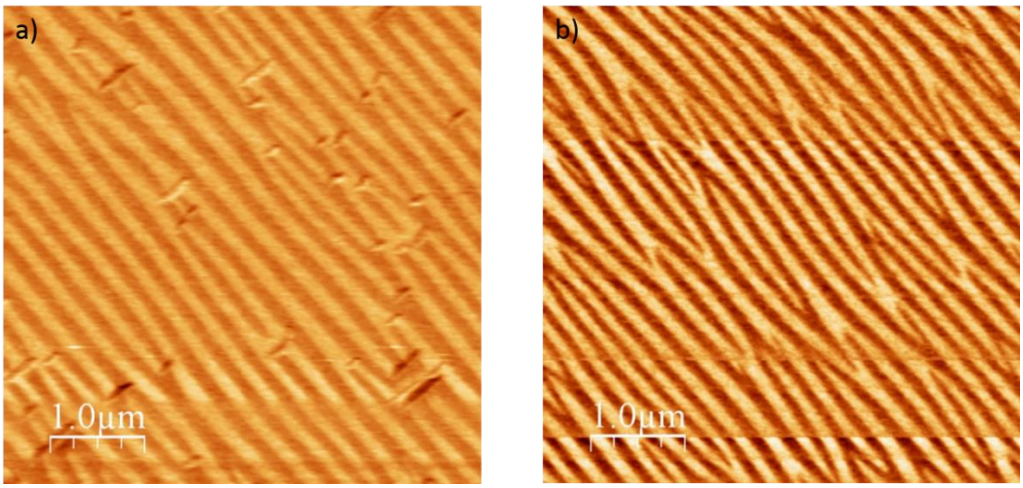

Figure 2.2 PFM images of the $BiFeO_3$ film a) with $SrRuO_3$ conducting layer and, b) without $SrRuO_3$ conducting layer.

2.2 Transmission electron microscopy (TEM) and Scanning transmission electron microscopy (STEM)

TEM has become a crucial instrument for investigating the characteristics of materials such as the nanostructure and the chemical composition. Imaging by TEM is the application of an electron beam with a wavelength in picometers through the samples to form the images. In TEM, the beam of electrons can undergo elastic or inelastic scattering with the atoms of the sample [66-68]. The scattered electrons would be diffracted according to the Bragg's law by the crystallographic orientation of the specimen. A diffraction pattern can be obtained at the back focal plane of the lens in the TEM and the pattern can provide the information about the lattice spacing and the atomic configuration of the specimen. For the beam of unscattered electrons, it will transmit through the specimen and provide a two dimensional image which is known as the bright-field image. As electrons are negatively charged, a specimen with more electrons around the nuclei will hence induce larger amount of electron scattering. Therefore, atoms with smaller atomic number will have a higher image intensity. Besides, the thickness of the sample will also affect the intensity of the images such that the thicker the specimen, the less electrons can be transmitted [69].

In addition, another mode of imaging in TEM is the high-resolution transmission electron microscopy (HRTEM). HRTEM provides a high magnification of the specimens at atomic scale by the phase contrast between the scattered electron beam and the transmitted electron beam. The phase contrast is aroused from the interference of the electron wave and it is unnecessarily correlated to the actual atomic structure of the specimens [70-72]. Even though HRTEM can provide a high resolution image of the specimen, there are some disadvantages such as the influence of the objective lens aberrations and the heavy dependence on the thickness of the specimens.

Comparing with HRTEM, scanning transmission electron microscopy (STEM) is extensively applied to study the atomic structure of the specimens such as ferroelectric materials due to its better image contrast. In STEM, a fine electron beam is focused and scanned over the specimen while parallel to the optical axis. There are two types of imaging modes in STEM which are the bright field imaging and the annular dark field imaging. For the dark field imaging, the scattered electron beam is detected by the annular detector and provides an atomic resolution image with intensity directly proportional to the atomic number (Z). However, light elements with low Z are not visible in dark field imaging. Therefore, the bright field

technique can be applied for both heavy and light elements imaging. In bright field imaging, the transmitted electron beam is obtained by the detector. For heavier atoms, the incident electrons will be scattered to a greater angle, therefore, the corresponding spots will be darker in the image [73-75]. The bright field imaging is usually used to provide complementary information for dark field imaging and hence STEM can be used to locate the corresponding positions of the atoms in ferroelectric materials.

2.3 Aberration-corrected scanning transmission electron microscopy (STEM)

Z-contrast dark field imaging

The atomic scale structure and polarization arrangement of $BiFeO_3$ were investigated using aberration-corrected STEM *Z*-contrast dark field imaging with sub-Ångstrom resolution.

For *Z*-contrast dark field imaging, the incident electron beam is scattered to high angles which is known as the high angle annular dark field (HAADF) image. There is no interference effect for the imaging, as a result, the HAADF images can be interpreted easily. The intensity of the HAADF is directly proportional to the atomic number and only heavy cations such as Bi and Fe cations are visible. As this

imaging has the advantages of no required post-processing and less sensitive to the samples thickness, therefore, the positions of heavy cations (Bi and Fe) can be precisely determined in *Z*-contrast images. In this work, the samples were prepared by focused-ion beam with standard procedures. In addition, the STEM images were taken by a doubled aberration corrected FEI Titan 80-300 FEG-TEM/STEM with the operating voltage of 300 kV and the HAADF images were taken with the collection angle of around 76 mrad.

2.4 Polarization and lattice parameters mapping

The STEM images were examined by customized Matlab image analysis using 2D peak-finding algorithm to determine the atomic positions of cations. Bi cations in the STEM images were used to calculate the lattice parameters and the central positions of individual unit cells. Fe cations were used to derive the displacement from the unit cell centres. In the HAADF images, the brighter dots represent the Bi cations and the darker dots represent the Fe cations. This is because Bi cation is heavier than Fe cation, so the image intensity of Bi cations will be higher. In order to locate the positions of all Bi and Fe cations, the noise was first eliminated from the HAADF STEM images. Next, the centre of mass of every bright spot in the

HAADF STEM images was identified automatically by the customized Matlab script for defining the feature locations. The Bi and Fe cations can then be distinguished by determining the size distribution of the identified spots. As the oxygen anions are not visible in the HAADF STEM images, therefore, the exact polarization of the unit cells cannot be directly visualized. However, the polarization can be derived by the displacement of the Fe cations. By comparing the marked Fe cations' positions and the central positions calculated by the four corner Bi cations' positions, the displacement vectors D_{FB} of Fe cations can be measured. The detailed procedures of locating the Bi cations, Fe cations and calculated central positions of the unit cells are illustrated in Figure 2.3a) to d). The polarization vectors are linearly proportional to the displacement of Fe cations by the equation of $P_s = -\frac{1}{V}\sum_i D_{FB} Z_i$ [18, 35, 76-77], where P_s is the polarization, V is the volume of unit cell, D_{FB} is the displacement vector and Z_i is the effective charge of the atom. As the displacement vectors are towards the negatively charged oxygen, therefore the polarization vectors are in the opposite directions which give rise to the negative sign of the equation. The polarization configuration maps will be obtained by mapping the opposite directions of the displacement vectors. Besides, the lattice parameters of the unit cells were measured by the distance between two

neighbouring Bi cations' along [100] and [001] directions separately. Hence, the direct lattice parameter maps along [100] and [001] directions can be obtained with the lattice parameters in Å represented by the colours.

Therefore, by examining the positions of Bi and Fe cations in the HAADF STEM images, both unit cell structure and the polarization vectors were mapped unit cell by unit cell. The relationship between polarization vectors and lattice parameters were also illustrated using the maps.

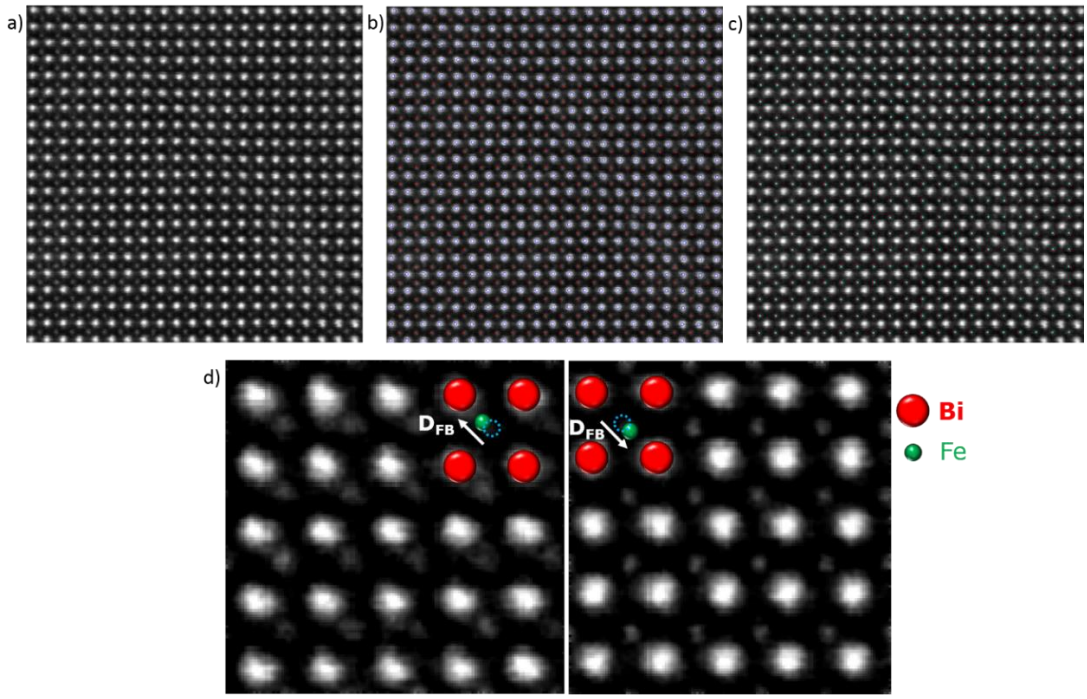

Figure 2.3 The schematic diagram of a) HAADF STEM image of $BiFeO_3$ thin film, b) locating the Bi cations and Fe cations which are represented by the blue dots and red dots respectively, c)

calculating the central positions which is indicated as the pale blue dots and d) calculating the $D_{FB.}$

Chapter 3 Atomic scale structure variation at ferroelectric domain walls

3.1 Introduction

Recent researches have demonstrated the novel properties of ferroelectric domain walls in $BiFeO_3$ thin films such as the enhanced electric conductivity and magnetization at the ferroelectric domain walls based on the coupling between electric and magnetic behaviors [78-80]. Owing to the fascinating application potential of $BiFeO_3$ in the electronic industries such as photovoltaic and ferroelectric memory devices [79], it is crucial to understand the underlying domain wall structure and the selection of different domain structures. A significant amount of study has been carried out to examine the domain architecture of 71°, 109° and the charged domain walls (CDWs), both experimentally and theoretically[31, 43, 81]. For instance, a massive amount of research has been carried on the mechanism of CDW formation and its atomic structure. A CDW is a domain wall formed by the 'tail to tail' or 'head to head' polarization configuration, so there are net charges accumulated at the domain wall. Li et al. [47] have reported the existence of the CDWs at 109° and 180° domain wall junctions using the HAADF STEM imaging

and found that these CDWs adopt the tetragonal-like structure locally, instead of the intrinsic rhombohedral structure. However, there is still inadequate research on the neutrally charged 180° domain walls using the atomic resolution STEM and the direct observation of structural variations at the domain walls.

3.2 Formation of 180° ferroelectric domain walls over 71° and 109° ferroelectric domain walls

The domain configurations were investigated by *Z*-contrast HAADF STEM imaging. From the HAADF STEM images, the polarization vector maps of $BiFeO_3$ were obtained and the boundary which separates two domains with different polarization orientations is defined as the domain wall. Figure 3.1a) shows the *Z*-contrast STEM image of the $BiFeO_3$ film in (010) plane where vector *a* and *c* represent the [100] and [001] direction. The polarization configuration map of $BiFeO_3$ is shown in Figure 3.1b) which labels the domain wall as the red area. The quantitative magnitude of the polarization vector is calculated by the simplified equation of $P_s = -2.5\frac{\mu C}{cm^2 \cdot pm} D_{FB}$ proposed by Nelson's group [35] where the 2.5 indicates the effective charges of the unit cell. As the measured displacement of the Fe cation is 30.7 ± 3.3 pm along the diagonal of the unit cell, the corresponding

image plane polarization is calculated to be 76.75 ± 8.25 μC/cm^2 with an equivalent polarization of 54.27μC/cm^2 in both [100] and [001] directions. In the assumption of the same polarization component of 54.27 μC/cm^2 in [010] direction which is normal to the image, the total polarization of the unit cell is estimated to be 94 μC/cm^2 which is consistent with the typical polarization magnitude of 90 μC/cm^2 to 100 μC/cm^2 for $BiFeO_3$. On the other hand, the polarization vectors of the two domains are obviously in opposite directions and lead to a 'head-to-tail' polarization configuration at the domain wall as shown in Figure 3.1b). It is revealed that the domain wall is 45° inclined instead of vertical. As stated in Chapter 1.4, the formation of domain walls should be mechanically and electrically compatible. Therefore, the 45° inclined domain wall can only be the 71° or 180° domain wall. However, the polarization vectors of the two neighboring domains projected in (010) plane should be the same for the 71° domain wall. Therefore, the domain walls obtained in this work should be the 180° domain wall since the polarization vectors of two neighboring domains projected in (010) plane are in opposite directions. In addition, we have investigated more than 10 HAADF STEM images of the neighboring regions and some of the examples are shown in Figure 3.2. It is

observed that the ferroelectric 180° domain wall is obtained and the domain walls are lamellae-patterned.

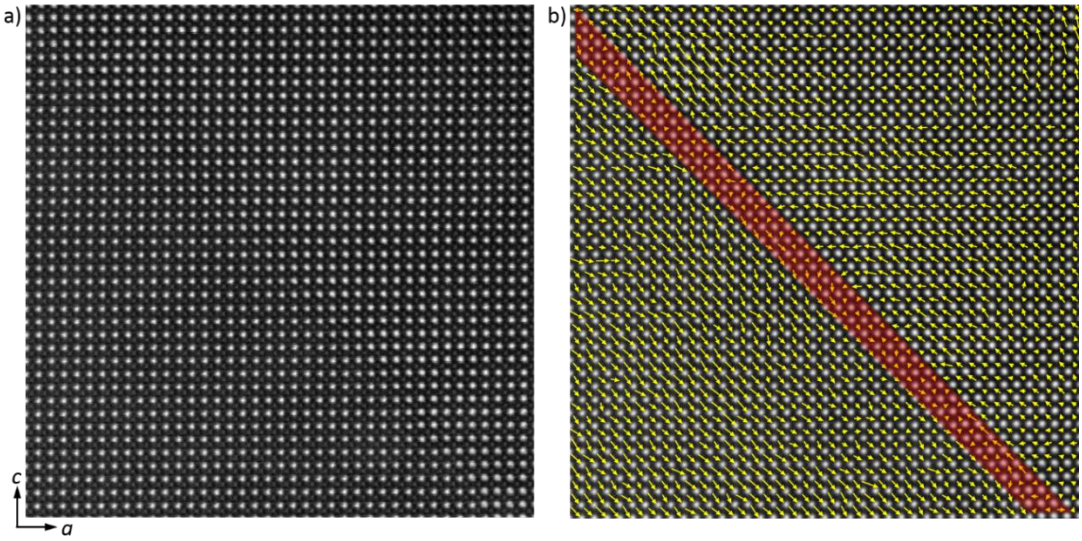

Figure 3.1a) *Z*-contrast STEM image of the $BiFeO_3$ film in (010) plane and b) Domain configurations with the 45° inclined 180° domain wall labeled by the red area.

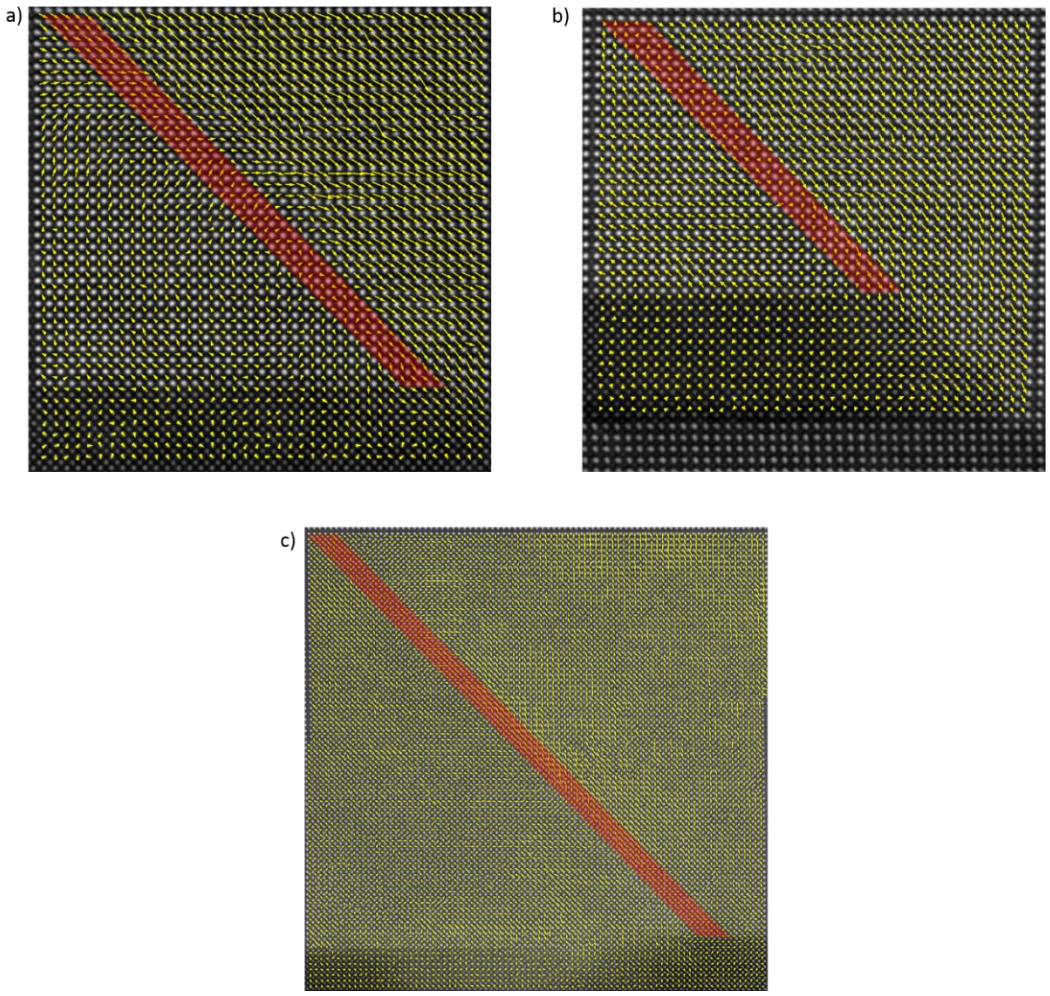

Figure 3. 2 a-c) HAADF STEM images of different neighboring 180° domain walls of the $BiFeO_3$ film in (010) plane.

Moreover, the mechanism of forming 180° domain walls instead of 71° and 109° domain walls is also critical. It is found that in the presence of conducting layer, 45° inclined domain walls such as 71° and 180° domain walls are more favorable than the vertical 109° domain wall [32, 57]. Without considering ferroelectric polarization discontinuity at the substrate interface, the competition of

forming the 71° or 109° domain wall strongly depends on the electrostatic boundary condition and the elastic compatibility condition. A depolarization field will be formed by the bound charges of the domains at the substrate interface. If the depolarization field is unscreened, it will increase the electrostatic energy and hence destabilize the ferroelectric domains [34, 82-83]. For a 109° domain wall, it has an alternating upward and downward directions of spontaneous polarization and it can reduce the depolarization field (if unscreened) at the substrate interface. However, the spontaneous polarization across a 71° domain wall is consistently upward or downward. Therefore, the 109° domain wall is more stable in the absence of the electrode that can provide charges to screen the depolarization field. In the view of elastic energy, as the 109° domain wall has a larger angle difference between the two neighboring ferroelastic domains while that of the 71° domain wall is smaller. As a result, the 71° domain wall has a lower elastic energy compared with that of the 109° domain wall.

It has been reported that the thickness of the $SrRuO_3$ has an influence on the metallicity and hence affect the formation of different types of domain walls [84-85]. With a smaller thickness of $SrRuO_3$ bottom electrode, the metallicity of $SrRuO_3$ decreases and results in less free electrons to reduce the depolarizing field.

Therefore, in the absence of or with an ultrathin (0-5 nm) $SrRuO_3$ bottom electrode, the 109° domain wall is more favorable than the 71° domain wall which can be explained by the lower electrostatic energy of the 109° domain wall associated with the lower depolarizing field.

In contrast, the 71° domain wall is expected to form in the presence of a $SrRuO_3$ conducting layer with a thickness larger than 25nm [32]. As the number of free carriers in the $SrRuO_3$ conducting layer increases with the $SrRuO_3$ film thickness, the depolarizing field can be fully screened by the free carriers of the $SrRuO_3$ conducting electrode. Besides, the 109° domain wall has a larger angle difference between the two neighboring ferroelastic domains while that of the 71° domain wall is smaller. As a result, when the depolarizing field is nearly fully screened by the thick $SrRuO_3$ layer, the 71° domain wall is more favorable to form as it has a lower elastic energy compared with that of the 109° domain wall.

It is also reported that 180° domain walls are usually obtained together with the formation of 109° domain walls [32]. However, we observed pure ferroelectric 180° domain wall array patterns without the presence of 109° domain walls with the presence of $SrRuO_3$ bottom electrode. The possibility of stabilizing 180° domain walls in $BiFeO_3$ grown on the $DyScO_3$ with $SrRuO_3$ (5 nm) bottom electrode were

mentioned by Crassous et al. [32]. As discussed above, the 109° domain wall is more favorable for an ultrathin or without the $SrRuO_3$ bottom electrode. Nevertheless, the effect of $BiFeO_3$ thin film thickness becomes critical when the $SrRuO_3$ thickness is 5 nm. Crassous's group demonstrated that for the $BiFeO_3$ thickness above 80 nm, the energy associated with the unscreened depolarizing field dominates due to the larger thickness (V = Ed), the formation of the 109° domain wall is still dominated as oppositely charged domain patterns can minimize the electrostatic energy. Nevertheless, the 71° domain wall is found to be obtained for the $BiFeO_3$ thickness less than or equal to 40 nm grown above the ultrathin $SrRuO_3$ bottom electrode with a thickness of 5 nm. It is the fact that for the thin film thickness less than or equal to 40 nm, the electrostatic energy due to the depolarizing field of the domain structure is not much (V = Ed). Therefore, the role of the elastic energy becomes dominant and the 71° domain wall which has a lower elastic energy is more preferable. Moreover, it can also be explained by the mechanical compatibility between the substrate and the two types of domain walls. As shown in Figure 1.10 and 1.11, the domains with 109° domain walls are puckered above the substrate due to the shear distortion, however, the domains are flat for 71° domain walls which can provide a better mechanical compatibility with the flat

substrate. Therefore, the enhanced accommodation of $BiFeO_3$ 71° domain structure also promotes the formation of the 71° domain wall over the 109° domain wall. Interestingly, for the $BiFeO_3$ thickness between 40nm and 80nm, a mixture of 71°, 109° and 180° domain walls is observed. It suggests that the 180° domain wall demonstrated in Figure 3.1 may be attributed to the effect of $BiFeO_3$ thin film thickness. In this work, the $BiFeO_3$ thin film with the thickness of 77 nm was grown on the $SrRuO_3$ bottom electrode. It shows the consistency with the work done by Crassous et al. which 180° domain walls can be stabilized for 40 to 80 nm $BiFeO_3$ film thickness. On the order hand, the formation of 180° domain walls is more likely to be favored by the interface termination and the detailed discussion will be established in Chapter 4.

3.3 Effect of $DyScO_3$ monoclinic distortion on the orientation of 180° domain walls

In addition, the HAADF STEM images were obtained at the $BiFeO_3/SrRuO_3/DyScO_3$ interface. Figure 3.3 demonstrates two different domain configurations with the 45° inclined domain wall at the substrate interface. As there is the presence of $SrRuO_3$ conducting layer, the vertical 109° domain wall is less

favorable to form. Instead, the 45° inclined domain wall with lower elastic energy is obtained. From Figure 3.3a), it shows that the 45° inclined 180° domain wall originated from the corner of the $SrRuO_3$ conducting island. Figure 3.3b) shows another 45° inclined 180° domain wall with a small horizontally-oriented region which can be considered as an intermediate region. It demonstrates the upward polarization above the $SrRuO_3$ conducting islands and downward polarization on the $DyScO_3$ substrate. Additionally, the polarization configurations at the domain wall maintain a 'head-to-tail' gradual change from the two oppositely polarized adjacent domains. This can ensure the charge neutrality of the 180° domain wall which is more energy favorable.

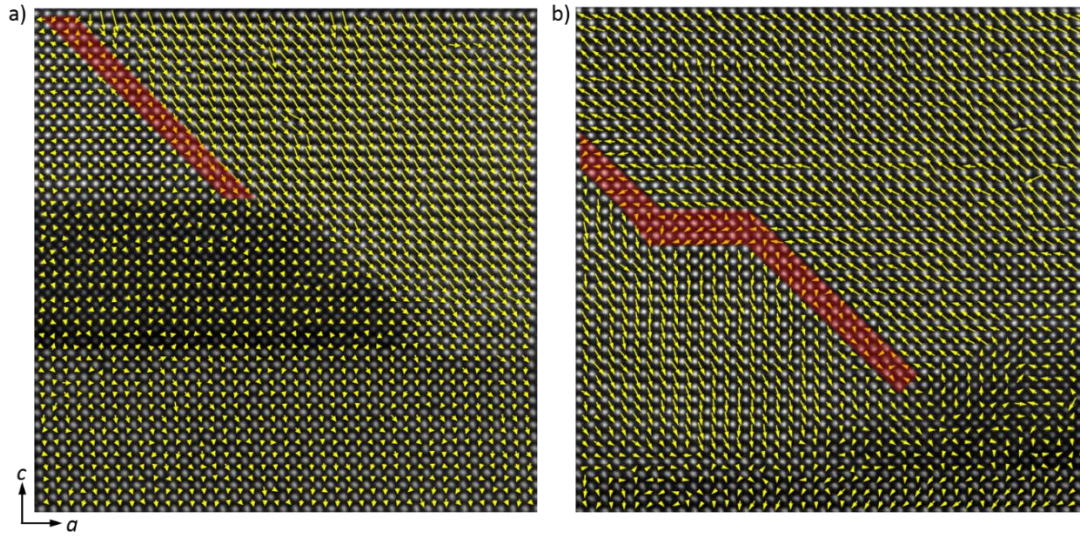

Figure 3.3 HAADF STEM image of a) the 45° inclined 180° domain wall, and b) the partially 45° inclined domain wall at $BiFeO_3/SrRuO_3/DyScO_3$ interface. The red area represents the region of domain wall.

Besides, it is evident that the 45° inclined domain wall is laid on the (101) plane of the $BiFeO_3$ thin film. This can be explicated by the monoclinic distortion of the $DyScO_3$ (110) substrate. As reported by Z. H. Chen et al. [86], the $BiFeO_3$ thin film will adopt the monoclinic distortion direction of the $DyScO_3$ substrate. In order to maintain an energetic favorable domain structure, the domain variants will be formed with a net shear distortion with respect to the monoclinic distortion of the $DyScO_3$ substrate. The schematic diagram of the $DyScO_3$ substrate viewed from $[001]_o$ direction with the monoclinic distortion along the upper left direction is

shown in Figure 3.4, where the subscript *o* denotes the orthorhombic structure. In Figure 3.5a), the domain wall is inclined along the (101) plane and labelled by the red dash line. In Figure 3.5b), the sub-diagram demonstrates the corresponding atomic configuration of the $DyScO_3$ substrate and reveals that the distortion of the $BiFeO_3$ unit cells is along the same direction as the monoclinic distortion of the $DyScO_3$ substrate. It is also displayed that the presence of $SrRuO_3$ conducting layer will not change such a distortion inheritance. These observations prove the consistency between our results and the previous works done by other researchers [55].

On the other hand, it has been reported that the formation of different domain structures can be controlled by the orientation of the substrate [48, 55, 56, 87]. Chu et al. found that [87] the ferroelectric symmetry would be broken by introducing the vicinal surface on the substrate. By increasing the miscut angle of the substrate, the types of domain variants will be reduced to maintain an energetically favorable condition. Besides, Giencke et al. [88] demonstrated that the miscut direction of the substrate can also restrict the formation of certain $BiFeO_3$ domain structure. With the occurrence of step edges on the growth substrate, it can prevent the formation of domains with unfavorable rhombohedral distortions. They also reported that the

miscut directions of the substrate will affect the alignment of different domain walls. However, in this work, the 180° domain walls with nearly the same orientation were observed on different sides of the $SrRuO_3$ island as shown in Figure 3.3. It is believed that the formation and the orientation of the 180° domain walls are mainly affected by other factors such as interface termination instead of the surface steps around the $SrRuO_3$ conducting islands.

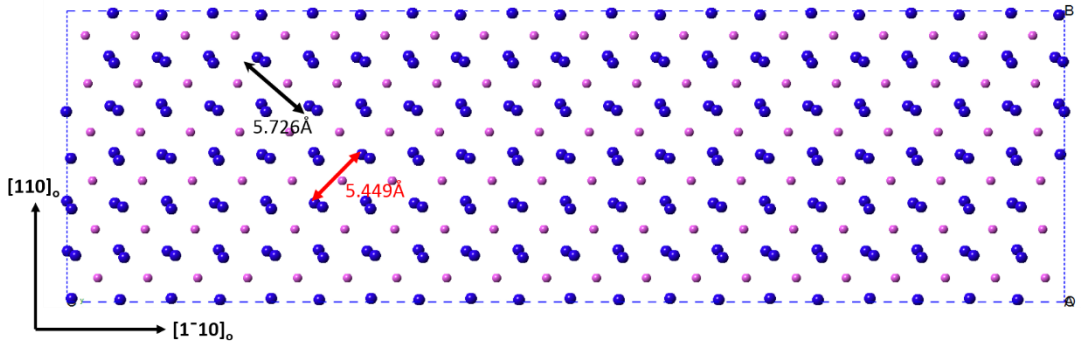

Figure 3.4 Schematic diagram of the $DyScO_3$ $(110)_o$ substrate viewed along $[001]_o$ direction.

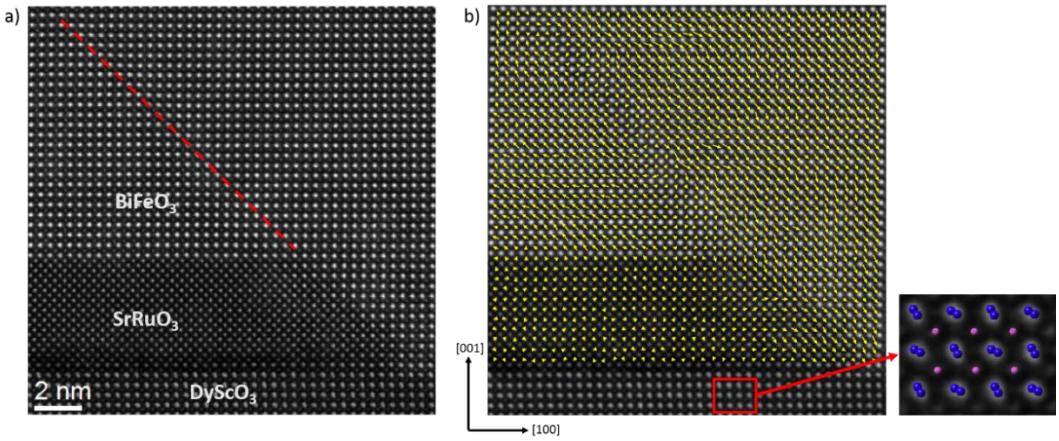

Figure 3.5a) HAADF STEM image of $BiFeO_3$ thin film with the inclined 180° domain wall labelled by the red dash line and b) the polarization vector map with the atomic configuration of the $DyScO_3$ substrate shown in the sub-diagram.

3.4 Ferroelectric polarization configuration and lattice parameter maps

Besides the observation and interpretation of 45° inclined 180° domain walls, the relationship between the polarization configurations and the lattice parameters was also studied. It is found that the polarization change at the domain walls will lead to the lattice distortions in both *a* and *c* direction.

Figure 3.6a) shows the HAADF STEM image of $BiFeO_3$ domains and the corresponding ferroelectric polarization vector map is shown in Figure 3.6b). Figure 3.6c) and d) represent the *a* and *c* lattice parameter maps respectively. It is demonstrated that the 45° inclined 180° domain wall leads to the expansion of

lattice spacing in *a* vector and the compression of lattice spacing in *c* vector when comparing with the lattice inside domains. Figure 3.6e) and f) show the line profiles of lattice parameters across the domain wall respectively. The lattice parameter changes across the domain wall can be explained by the displacement of Bi cations relative to the Fe cations sublattice. Polarization can also be defined as the displacement of Bi cations from the corner positions of the perovskite pseudocubic unit cells. Therefore, the polarization direction can be regarded as the displacement of Bi cations with respect to the Fe cation sublattice. This means that across a 180° domain wall, the Bi cation displacements in the two neighboring domains are along the two opposite polarization directions. The schematic model of Bi cations displaced from the corner positions of the pseudocubic perovskite unit cell across the domain wall is shown in Figure 3.7. The Bi pseudocubic unit cell in the bulk domains is denoted by the blue frame and the deformation of Bi unit cell is represented by the yellow frame. It is conspicuous that there is an expansion in *a* vector and compression in *c* vector. These are the results of the Bi sublattice of the two neighboring domains distorted away from the domain wall in *a* vector but distorted towards the domain wall in *c* vector. Therefore, the *a* lattice spacing of Bi cations across the domain wall increased while the *c* lattice spacing decreased. It

should be noted that the normal displacement vector of Bi cations with respect to the domain wall is zero. Therefore, the 180° domain wall can remain neutrally charged. In addition, from the ferroelectric polarization vector map, the width of the 180° domain wall is about two pseudocubic unit cells. It shows the agreement with the schematic model of Bi cations lattice distortion across the domain wall shown in Figure 3.6 and the result of Wang's group [19] that the thickness of the 180° domain wall is about two Fe/Bi columns width.

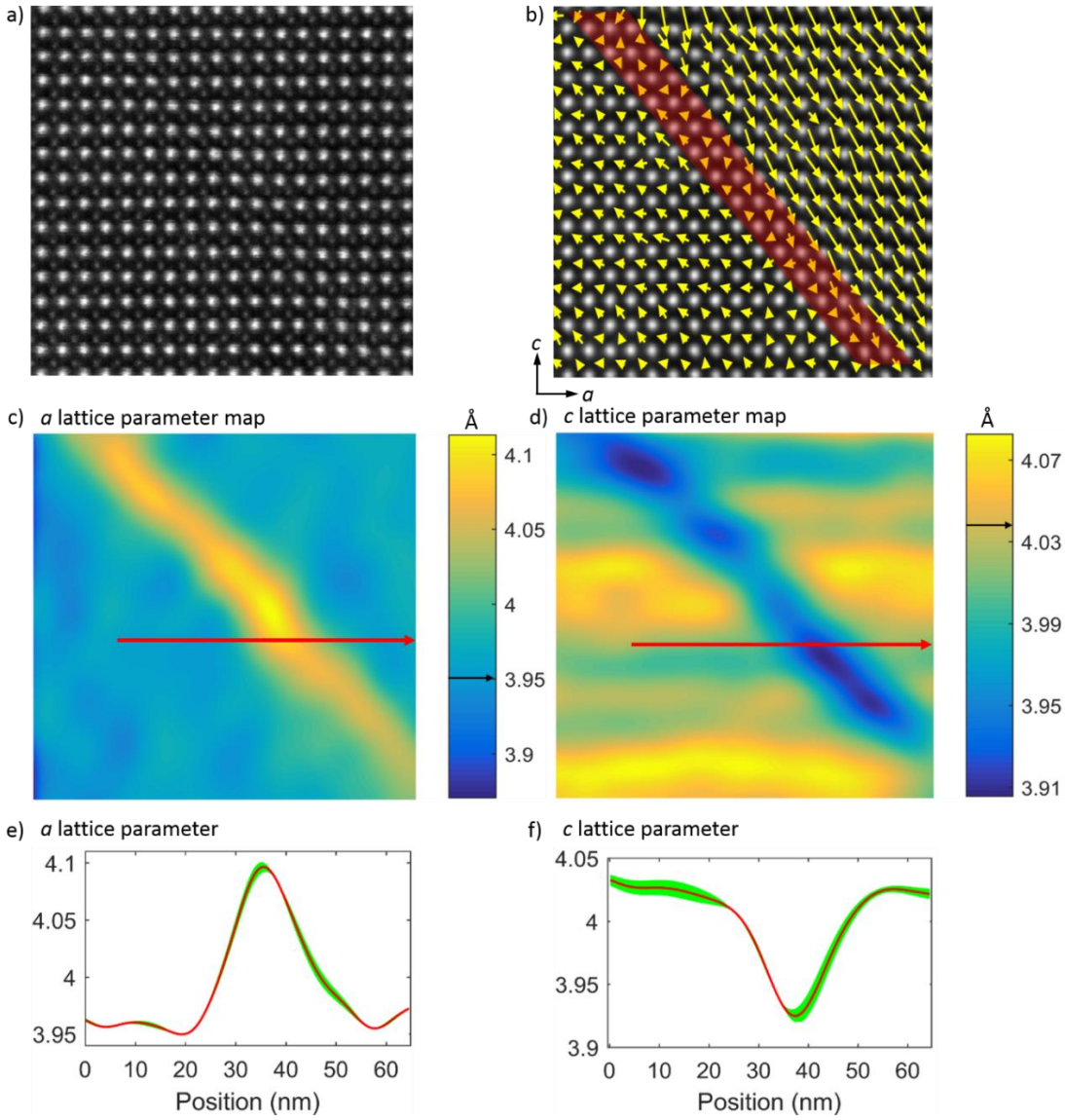

Figure 3.6a) HAADF STEM image of $BiFeO_3$ bulk domain, b) polarization configuration map of the 45° inclined 180° domain wall, where the red area indicates the region of domain wall, c) the *a* lattice parameter map, d) c lattice parameter map, e) and f) the lattice parameter changes across the domain wall in *a* vector and *c* vector respectively.

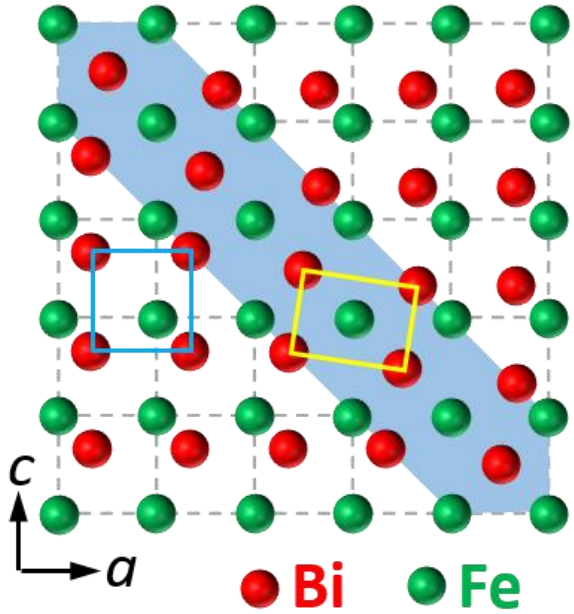

Figure 3.7 Schematic model of Bi cations distortion from the corner positions of the pseudocubic perovskite unit cell across the domain wall. The domain wall is labeled by the blue shadow area.

Furthermore, it has been discovered that there are two different types of polarization configurations across the 45° inclined 180° domain walls which are the clockwise and anti-clockwise polarization configurations. The comparison of the two types of polarization configurations and the relationship between the lattice spacing were examined. Figure 3.8a) shows the clockwise polarization configuration map and the corresponding *a* and *c* lattice parameter maps are shown in Figure 3.8c) and e) respectively. Similarly, the anti-clockwise polarization

configuration map is shown in Figure 3.8b) and the correlated *a* and *c* lattice parameter maps are shown in Figure 3.8d) and f). It can be realized that the *a* and *c* lattice spacing variations of clockwise and anti-clockwise polarization configurations are in opposite trend. For the clockwise polarization configuration, the *a* lattice spacing increases and *c* lattice spacing decreases. For the anti-clockwise polarization configurations, the *a* lattice spacing decreases and the *c* lattice spacing increases. This can be confirmed by the schematic model shown in Figure 3.7. In the case of anti-clockwise polarization configurations, the Bi cations of the two adjacent domains are displaced towards the domain wall in *a* vector but away from the domain wall in *c* vector.

This demonstrated that the domain structures can be tailored by controlling the epitaxial strain from the growth substrates. It has been reported that the compressive strain induced by the substrate to the $BiFeO_3$ thin film can suppress the formation of particular domain structures, and under the tensile strain, there is a rotation of the $BiFeO_3$ unit cell with the increase of thickness so that the strain can be partly released [55, 87, 89]. In this work, it is observed that for the anti-clockwise polarization rotation, the $BiFeO_3$ film is compressed horizontally as shown in Figure 3.8b). Therefore, it suggests that such polarization configuration of $BiFeO_3$ can be

more favored by choosing the substrates with smaller lattice parameters which provide a compressive strain on $BiFeO_3$.

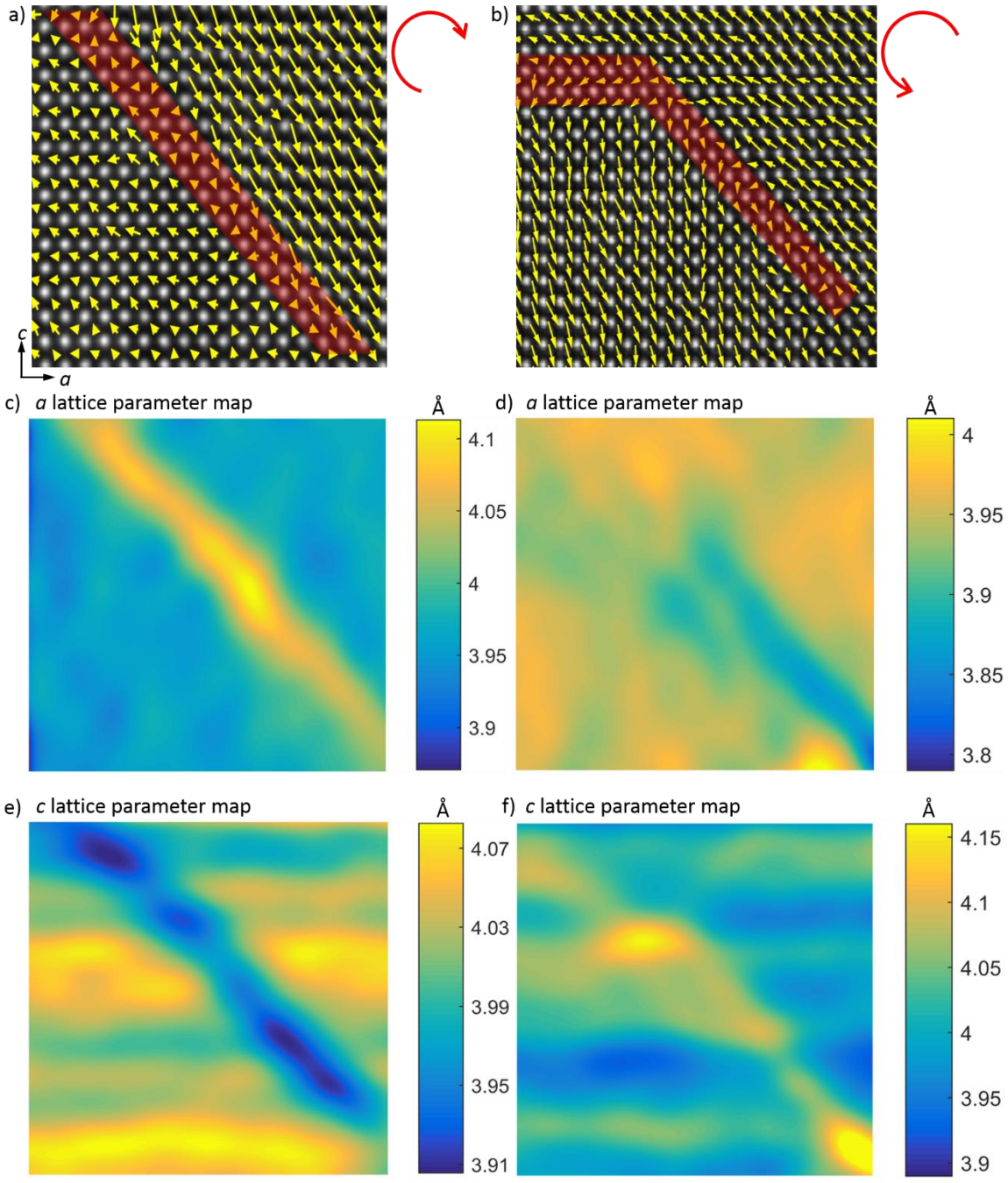

Figure 3.8 Polarization configuration maps of the 45° inclined 180° domain wall with a) clockwise polarization configuration and b) anti-clockwise polarization configuration, where the red area indicates the region of domain wall, the *a* lattice parameter map of c) clockwise

polarization configuration and d) anti-clockwise polarization configuration, *c* lattice parameter map of e) clockwise polarization configuration and f) anti-clockwise polarization configuration respectively.

3.5 Other intriguing ferroelectric polarization configurations

Other than the above polarization configurations across the domain walls, there are still some unusual domain patterns. The domain patterns were investigated by the polarization configuration mapping and the lattice parameter mapping.

Firstly, we observed a triangular vortex domain structure at the substrate interface with a $SrRuO_3$ conducting island from the polarization configuration map. From Figure 3.9a), there are three different types of polarization domains which are labelled as domain A, B and C. In addition, a 45° inclined 180° domain wall is formed between the domain region A and B. The polarization configurations of the two continuous domains undergo anti-clockwise rotation and the corresponding *a* and *c* vector lattice parameter maps are shown in Figure 3.9b) and c) respectively. It is demonstrated that the *a* lattice spacing decreases and the *c* lattice spacing increases at the domain wall. These variations in lattice parameter are consistent with the results of Chapter 3.3. Meanwhile, a triangular vortex domain is formed next to the $SrRuO_3$ island with a gradual clockwise rotation of polarization direction.

The white dash line indicates the transition from domain region B to domain region C. It appears that the polarization direction in domain C aligns with the side edge of the $SrRuO_3$ island, suggesting that such a vortex pattern is related to the morphology of the $SrRuO_3$ island.

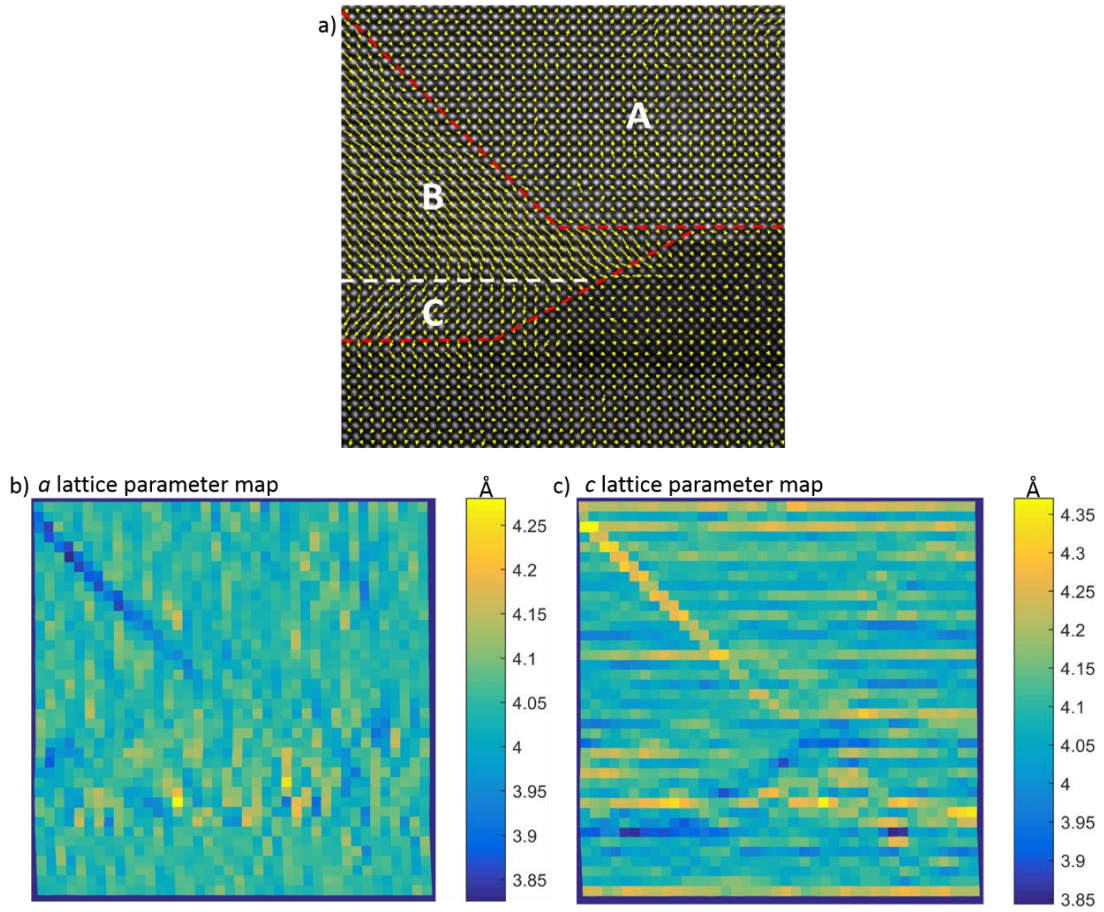

Figure 3.9a) Polarization vector map of vortex domain, b) *a* lattice parameter map and c) *c* lattice parameter map.

Secondly, it is found that there is another interesting polarization configuration next to the triangular vortex domain. From Figure 3.10a), the domain with upward polarization above the $SrRuO_3$ conducting layer is enveloped by the domain with downward polarization. The boundaries formed between the domains are 180° domain walls which acquire the same lattice parameter variations as mentioned above, as shown in Figure 3.10b) and c).

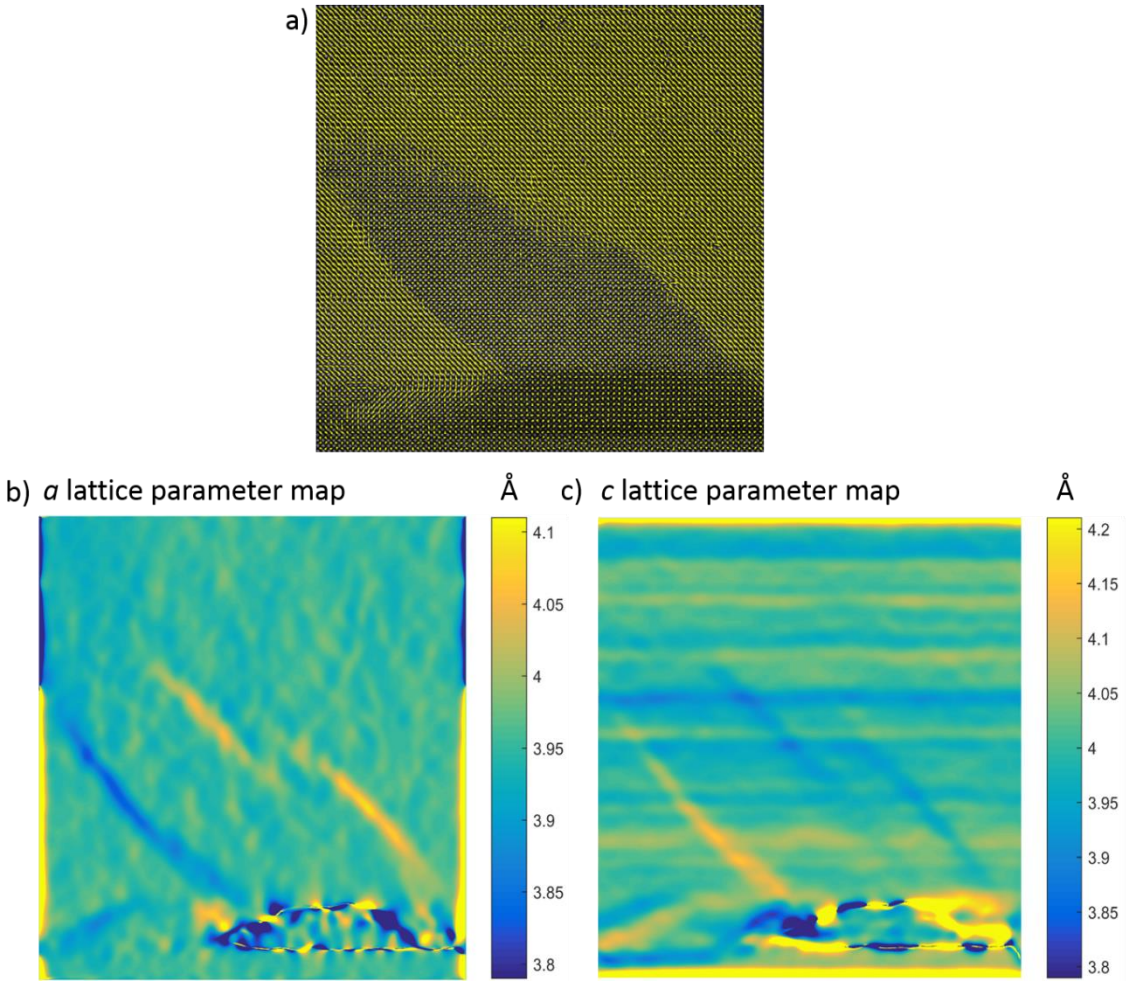

Figure 3.10a) Polarization configuration map of enveloped domain structure with 180° domain walls, b) *a* lattice parameter map and c) *c* lattice parameter map.

3.6 Conclusion

To conclude, we have successfully investigated the HAADF STEM images of ferroelectric domain structures of the $BiFeO_3$ thin film. We discovered that there are 45° inclined 180° ferroelectric domain walls formed above the $SrRuO_3$ bottom electrode and the orientation of the 180° domain walls are along the (101) plane.

Furthermore, it is revealed that the lattice parameters in *a* and *c* vectors vary at the 180° domain walls from the domains as discussed in Chapter 3.4. For the clockwise polarization configuration formed by the adjacent domains, the domain walls possess an increased *a* lattice spacing and a decreased *c* lattice spacing. On the contrary, the changes of *a* and *c* lattice parameters reversed for anti-clockwise polarization configuration. This is the result of the relative displacement of the Bi cations along different lattice vectors. This confirms the ferroelectric polarization in $BiFeO_3$ is mainly due to the Bi displacement relative to Fe and O. It is also proposed that the domain structures of $BiFeO_3$ can be affected by the mechanical strain introduced from the growth substrates. Besides, there are some unusual domain structures observed in the $BiFeO_3$ film. These can be further studied to provide a better understanding of the formation of ferroelectric domains.

The orientation of the 180° domain walls is mainly attributed to the monoclinic distortion of the $DyScO_3$ substrate such that the 180° domain walls are lying on the (101) plane. Besides, previous studies suggested that the distortions of the $BiFeO_3$ domains and the orientations of the domain walls will be influenced by the morphology of the $SrRuO_3$ bottom electrode such as the terrace alignment. However, we discovered the same orientation of domain walls at both edges of the $SrRuO_3$

island which indicates that the formation and the orientation of the 180° domain walls are independent of the surface morphology of the $SrRuO_3$ island. This provides a notable understanding on the mechanism of ferroelectric 180° domain walls formation.

Chapter 4 Ferroelectric domain engineering by interface terminations

4.1 Introduction

As mentioned in the previous chapter, we observed that the polarization vectors above the $SrRuO_3$ is pointing upward while the polarization vectors above the $DyScO_3$ is pointing downward. This is completely opposite to the majority of studies on $BiFeO_3$ ferroelectric polarization orientations which showed that the polarization direction is usually downward above the $SrRuO_3$ bottom electrode [55, 87-88, 90-91]. The downward polarization above the $SrRuO_3$ layer can be understood by the Schottky contact at the interface between the $BiFeO_3$ and $SrRuO_3$ [90, 92-93]. According to the Schottky Mott rule [94-96], as the work function of $SrRuO_3$ and the electron affinity of $BiFeO_3$ are 5.2 eV and 3.3 eV respectively, a Schottky barrier height of 1.9 eV will be formed at the interface and it can be regarded as a 'n type' Schottky contact. Therefore, a built-in electric field would be established pointing from $BiFeO_3$ to $SrRuO_3$ and the polarization direction would be pointing toward $SrRuO_3$. The schematic diagram of the Schottky Mott model and the formation of built-in electric field between $BiFeO_3$ and $SrRuO_3$ is illustrated in

Figure 4.1 where E_F, χ, Φ_{SB}, E and P denote the work function of $SrRuO_3$, electron affinity of $BiFeO_3$, the Schottky barrier height, electric field and polarization respectively. Surprisingly, however, the observed polarization direction above the $SrRuO_3$ bottom electrode in this work is pointing away from $SrRuO_3$ which is totally different from the mentioned mechanism. This is most likely due to the effect of interface termination on polarization direction.

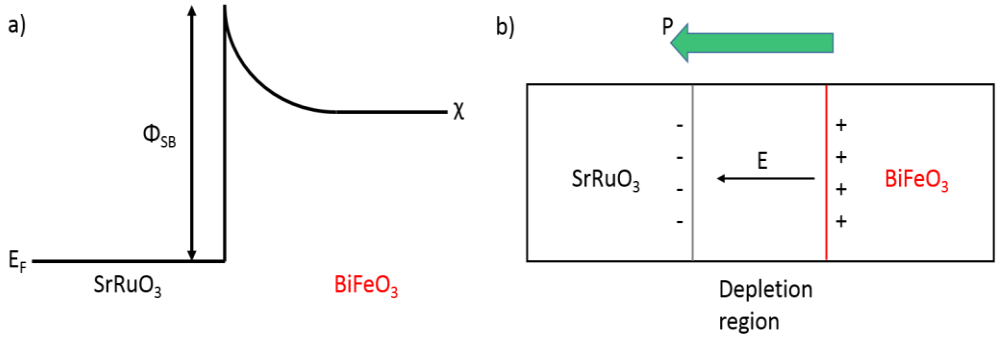

Figure 4.1 Schematic diagram of a) Schottky contact between $BiFeO_3$ and $SrRuO_3$ and b) built-in electric field across the depletion region.

Polarization discontinuity and the electrostatic boundary condition at the heterostructure interface should also be considered in the mechanism of the domain formation. It is because the atomic behaviors at the interface may differ from that of the bulk domains. Therefore, the opposite trend of polarization directions above

the $SrRuO_3$ bottom electrode and the $DyScO_3$ substrate can be examined by the effect of interface termination which may also contribute to the formation of the pure ferroelectric 180° domain walls.

4.2 Interface termination of $BiFeO_3$ and $SrRuO_3$ heterointerface

The atomic structure of $BiFeO_3/SrRuO_3$ interface was investigated by the HAADF STEM. The intensity profiles at the interface of different domain structures were obtained to study the interface termination and hence the effect of terminating atoms on polarization configurations. In the HAADF STEM image, oxygen anions are invisible while cations can be shown and the intensity will increase with the atomic weight of the element. Therefore, for the $BiFeO_3/SrRuO_3$ heterointerface, only Bi, Fe, Sr and Ru cations are shown in the HAADF STEM image and the intensity profiles were taken along the cross section of the heterointerface with the alternating layers of AO and BO_2. The intensity profile along the white line across the heterointerface with selected region labelled by the red box is shown in Figure 4.2, it is revealed that the peak of the intensity profile decreases with the sequence of Bi > Ru > Sr > Fe according to their atomic weights. In the $BiFeO_3$ thin film, the higher peaks correspond to the Bi cations while the lower peaks correspond to the

Fe cations. Similarly, the higher peaks are the Ru cations and the lower peaks are the Sr cations in the $SrRuO_3$ bottom electrode. It is can be seen the layer between BiO and SrO should be RuO_2 as the intensity is much higher than that of FeO_2. Therefore, it is RuO_2 terminated (B site termination) above the $SrRuO_3$ bottom electrode.

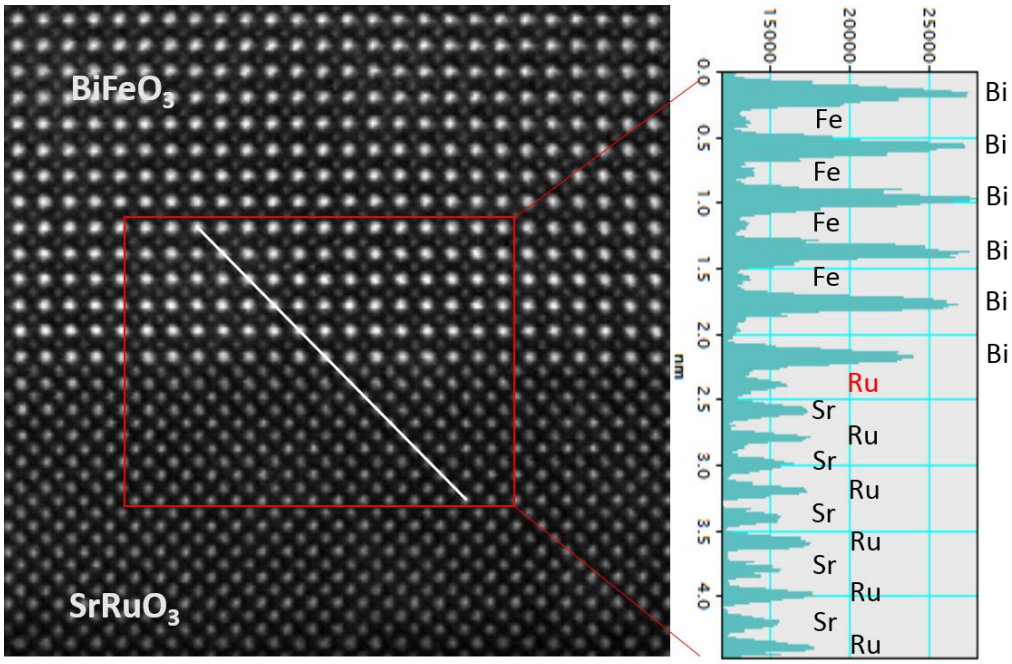

Figure 4.2 The intensity profile across the $BiFeO_3/SrRuO_3$ heterointerface with RuO_2 terminating layer.

The polarization direction pointing from the $SrRuO_3$ bottom electrode to the $BiFeO_3$ film (upward) can be explained by the polarization discontinuity model. Various researches have successfully demonstrated the influence of interface

termination to the polarization direction resulting from the polarization discontinuity at the heterostructure interface [92, 97-98]. As the structure of ABO_3 perovskite material can be seen as the stack of AO and BO_2 alternating layers, therefore, the interface termination can be defined by the terminating layer of the bottom electrode or the substrate [99-100]. There are two types of interface termination which are the A site termination with AO terminating layer and B site termination with BO_2 terminating layer. N. Nakagawa et al. [101] found that at the complex oxide interface with different interface terminations, charge rearrangement or atomic reconstruction such as oxygen vacancies at the interface would be required to accommodate the polar discontinuity at the interfaces. They proposed that in order to prevent electrostatic potential divergence with the increase of film thickness, charge rearrangement would occur for 'n-type' interface with Ti-O termination, in which the excess electrons e^- are denoted to the mixed valence states substrate layer from the polar thin film through the interface. In contrast, for the 'p-type' interface with Sr-O termination, oxygen vacancies would be introduced to the substrate layer at the interface. Hence, for both 'n type' and 'p type' interface, electrostatic potential divergence can be avoided.

In addition to the elimination of electrostatic potential divergence, interface termination can also determine the direction of polarization at the interface. P. Yu et al. [102] have demonstrated the dependence of polarization direction on the interface termination between the ferroelectric $BiFeO_3$ thin film and $La_{0.7}Sr_{0.3}MnO_3$ (LSMO) conducting layer. It is suggested that the polarization direction is pointing to the bottom electrode from the $BiFeO_3$ (downward) for the $La_{0.7}Sr_{0.3}O$ terminated layer (A site termination) at the $La_{0.7}Sr_{0.3}O/FeO_2/BiO$ interface. Conversely, for the MnO_2 terminated layer (B site termination) at $MnO_2/BiO/FeO_2$ interface, the polarization direction is pointing to the $BiFeO_3$ from the bottom electrode (upward). This can be elucidated by the polarization discontinuity model at the interface where the $La_{0.7}Sr_{0.3}O$, MnO_2, BiO and FeO_2 layer carry a charge density of +0.7e, -0.7e, +1e and -1e respectively. For the $La_{0.7}Sr_{0.3}O$ termination, the valence mismatch between the $La_{0.7}Sr_{0.3}O$ and FeO_2 is -0.3e and the interface is negatively charged. Therefore, the polarization vector is pointing from the interface to the bottom electrode (downward). In contrast, for MnO_2 termination, the interface is positively charged and the valence mismatch is +0.3e. Hence, the polarization direction is pointing from the bottom electrode to the interface (upward).

By using the same polarization discontinuity model, it can be applied to explain the unusual polarization configurations above the $SrRuO_3$ conducting layer as well as that of the $DyScO_3$ substrate obtained in this work. The schematic diagram of the $RuO_2/BiO/FeO_2$ interface model is shown in Figure 4.3. It is demonstrated that the valence mismatch between the RuO_2 and the BiO^+ layer is +1 and the nominal charge density at the RuO_2 terminated interface is positive. Therefore, the polarization vector is pointing from the $SrRuO_3$ bottom electrode to the $BiFeO_3$ film (upward). In addition, other $BiFeO_3/SrRuO_3$ heterointerface regions shown in Figure 4.4 were also studied to confirm the upward polarization configurations induced by the RuO_2 terminated layer.

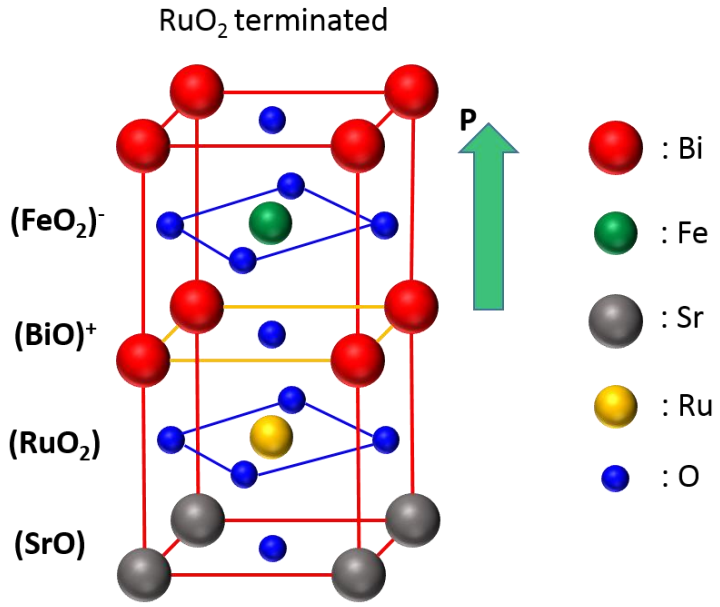

Figure 4.3 Schematic diagram of the $RuO_2/BiO/FeO_2$ heterointerface model with upward polarization.

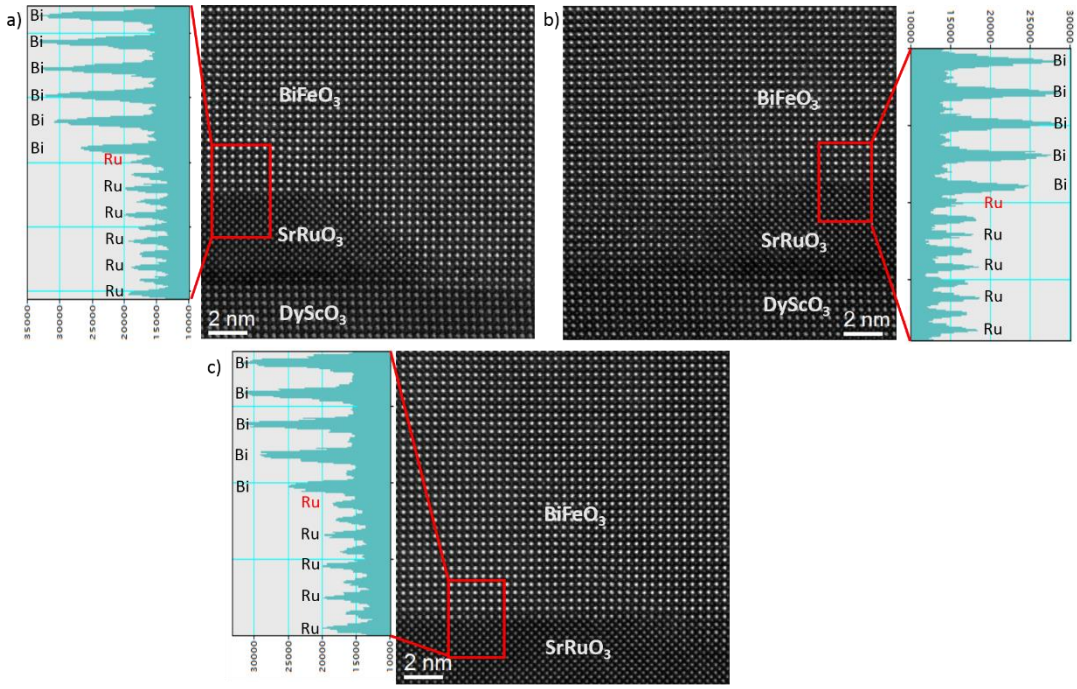

Figure 4.4 The intensity profile across the $RuO_2/BiO/FeO_2$ interfaces with RuO_2 terminating layer at different $BiFeO_3/SrRuO_3$ interfaces.

4.3 Interface terminations at $BiFeO_3/DyScO_3$ heterointerface

Conversely, it is indicated that the polarization direction of $BiFeO_3$ domains directly above the $DyScO_3$ substrate (no $SrRuO_3$) is pointing from the $BiFeO_3$ to the interface (downward). The intensity profiles of the HAADF STEM images were used to investigate the atomic arrangement of the $BiFeO_3/DyScO_3$ interface. Referring to atomic mass of the four cations, the peak intensity should be decreasing in the order of Bi > Dy > Fe > Sc. From Figure 4.5, it shows the intensity profile of the HAADF STEM image across the $BiFeO_3/DyScO_3$ heterointerface labelled by the red frame. Surprisingly, the intensity drops at the interface which does not correspond to BiO or DyO layer. It can be proposed that the intensity is due to the existence of SrO layer during the growth of $SrRuO_3$ island nearby. As the atomic mass of Sr cation is smaller than both Bi and Dy cations, therefore, it shows the consistency of the two lower peaks in the intensity profile. Even though the terminating layer of the $DyScO_3$ substrate is ScO_2 (B site), the additional SrO layers alter the interface layer arrangement to be $SrO/FeO_2/BiO$ and hence the heterointerface becomes SrO termination (A site). In order to prove the existence of the SrO layers, the energy dispersive X-ray spectroscopy (EDXS) has been conducted at the $BiFeO_3/DyScO_3$ heterointerface. From Figure 4.6, it shows the

atomic resolution EDXS map at the $BiFeO_3/DyScO_3$ heterostructure. It is obvious that there are layers of SrO between the $BiFeO_3$ film and the $DyScO_3$ substrate. It can justify the occurrence of SrO termination and the atomic arrangement of the heterointerface layers becomes $SrO/FeO_2/BiO$.

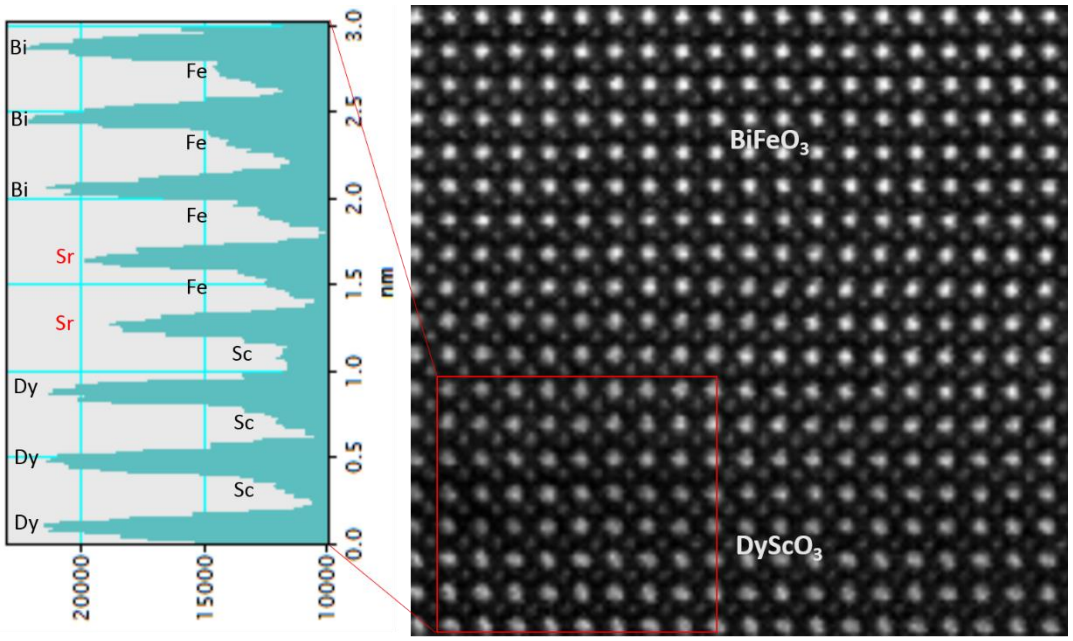

Figure 4.5 The intensity profile across the $BiFeO_3/DyScO_3$ heterointerface with SrO terminating layer.

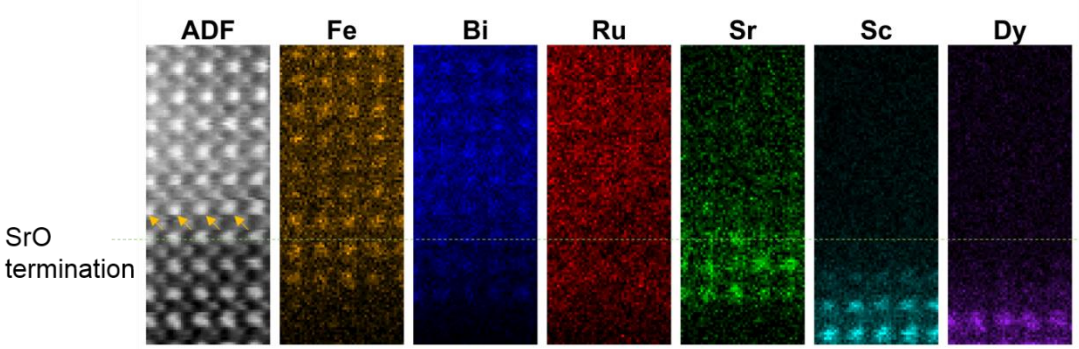

Figure 4.6 Atomic resolution EDXS map at the $BiFeO_3/DyScO_3$ heterostructure.

The schematic diagram of the polarization discontinuity model of $SrO/FeO_2/BiO$ heterointerface is shown in Figure 4.7 and it explains the mechanism of polarization vectors pointing from the $BiFeO_3$ film to the interface (downward). The valence mismatch at the interface becomes -1 because of the presence of SrO terminating layer which carries zero electrostatic charge and the $SrO/FeO_2^-/BiO^+$ has a negative nominal charge density. As a result, the polarization vector is pointing from the interface to the $DyScO_3$ substrate. Additionally, the intensity profiles at other $BiFeO_3/DyScO_3$ interfaces also demonstrate the SrO termination at the interface and are presented in Figure 4.8. The *M* letter in the intensity profile indicates the possible mixed layers of BiO and DyO. Nonetheless, the presence of SrO layer still contributes to the downward polarization towards the $DyScO_3$ substrate. It is believed that the opposite polarization directions induced by the interface terminations at the $BiFeO_3/DyScO_3$ and $BiFeO_3/SrRuO_3$ interfaces must contribute to the formation of 180° domain walls. It also suggests that the nucleation sites of the domain walls can be preferentially controlled by the interface terminations.

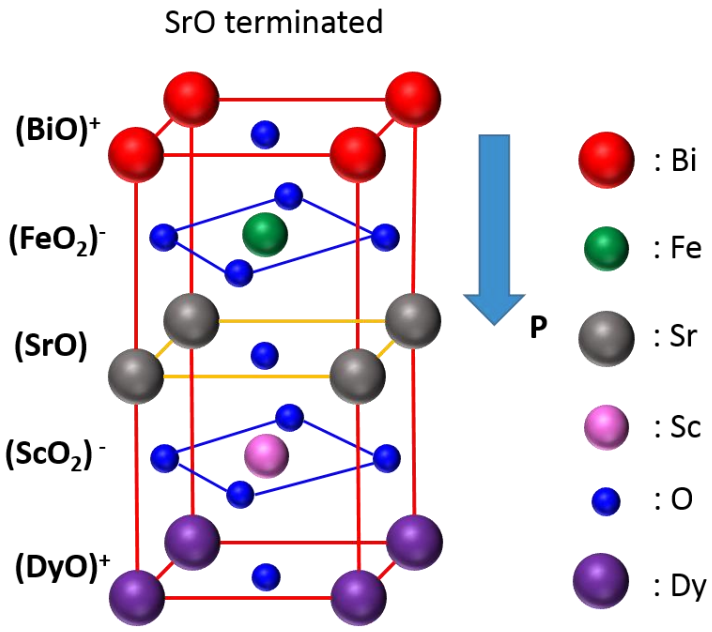

Figure 4.7 Schematic diagram of the SrO/FeO_2/BiO heterointerface model with downward polarization.

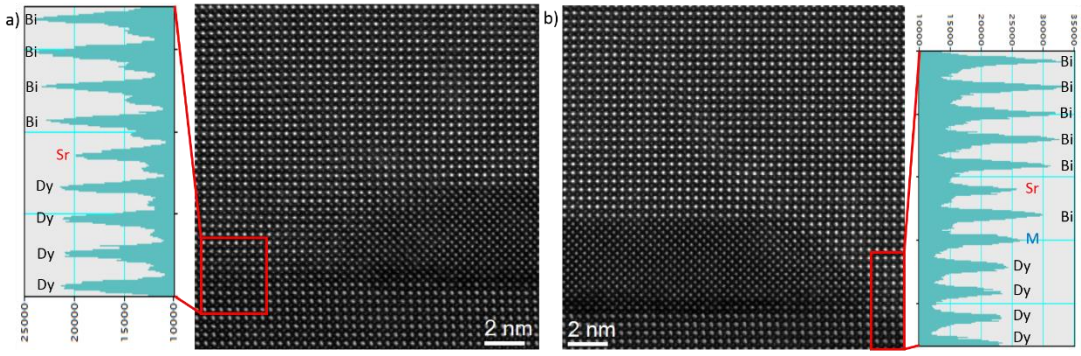

Figure 4.8 The intensity profile across different SrO/FeO_2/BiO interfaces with SrO terminating layer.

4.4 Conclusion

To conclude, the polarization configurations above the $SrRuO_3$ bottom electrode and $DyScO_3$ substrate were examined by the polarization discontinuity model at the heterostructure. The intensity profile of the HAADF STEM images demonstrate the interface termination of the heterostructure alternating layers. It is observed that the $BiFeO_3/SrRuO_3$ heterointerfaces are RuO_2 terminated which shows a positive charge density and leads to the upward polarization direction from the bottom electrode to the $BiFeO_3$ film. Additionally, the intensity profile of the HAADF STEM images and EDXS mapping demonstrate the occurrence of additional SrO layers at the $BiFeO_3/DyScO_3$ interfaces which results in a negative charge density and hence the downward polarization at the heterointerface.

The opposite polarization directions aroused by the interface terminations of $BiFeO_3/SrRuO_3$ and $BiFeO_3/DyScO_3$ at the edge of the $SrRuO_3$ island reveal the nucleation sites of 180° domain walls. It is believed that ferroelectric 180° domain walls can be artificially obtained by controlling the interface terminations which may be valuable for the future electronic applications.

Chapter 5 Conclusions and future work

5.1 Conclusions

In this work, the aberration corrected HAADF STEM images of the $BiFeO_3$ thin films have been successfully investigated. The atomic scale structure of the ferroelectric $BiFeO_3$ domains together with domain walls were studied by mapping the polarization configurations and the lattice parameters of the $BiFeO_3$ thin films using the customized Matlab image analysis program with 2D peak-finding algorithm. The polarization configuration maps demonstrate that the 45° inclined 180° domain walls lying on (101) plane were obtained above the $SrRuO_3$ bottom electrode 'islands'. The incline direction of the 180° domain walls is mainly attributed to the $DyScO_3$ substrate monoclinic distortion direction. The coherent distortion direction between the $BiFeO_3$ thin film and $DyScO_3$ substrate enable a favorable energetic stability for the domain structures. Additionally, it is proposed that the surface morphology of the $SrRuO_3$ will not affect the formation of the domain walls. It is also observed that there are two types of polarization configurations across the 180° domain walls which are the clockwise and anti-clockwise polarization configurations. Moreover, the relationship between

polarization configurations and lattice parameter variations at the domain walls are established by examining the lattice parameter maps. For the 180° domain walls with clockwise polarization configurations, the *a* lattice parameters increase and the *c* lattice parameters decrease across the domain wall. On the contrary, the lattice parameter variations across the domain wall reverses for anti-clockwise polarization configurations. The lattice spacing variations at the 180° domain walls are due to the relative displacement of the Bi cations in the perovskite unit cell driven by the ferroelectric polarization. It also suggests that the domain structures can be controlled by strain engineering. Besides, a triangular vortex domain near the $SrRuO_3$ bottom electrode was also demonstrated by polarization configuration mapping which needs further study.

Additionally, the polarization configurations above the $SrRuO_3$ bottom electrode are found to be in upward direction which is opposite to other studies. This is elucidated by interface termination based on the polarization discontinuity model. Intensity profile of the HAADF STEM images are acquired to evaluate the atomic arrangement of the heterostructure alternating layers. It is revealed that the $BiFeO_3/SrRuO_3$ heterointerface is RuO_2 terminated which leads to a positive charge density at the interface and hence the polarization vector is pointing from the bottom

electrode to the $BiFeO_3$ film (upward). The interface termination at the $BiFeO_3/DyScO_3$ interfaces are also studied. It is discovered that there are additional SrO layers between the $BiFeO_3$ thin film and $DyScO_3$ substrate by both STEM imaging and EDXS mapping. The occurrence of SrO layers contributes to the downward polarization at the $BiFeO_3/DyScO_3$ interface as the interface becomes SrO terminated and possesses nominal negative charge density. The oppositely oriented polarization configurations induced by the $BiFeO_3/SrRuO_3$ and $BiFeO_3/DyScO_3$ interface terminations explain the formation of the 180° domain walls at the edge of the $SrRuO_3$ bottom electrode.

5.2 Future work

The atomic scale structure variations at the 180° ferroelectric domain walls of $BiFeO_3$ multiferroic material have been successfully investigated. The polarization vector maps and lattice parameter maps reveal the relationship between polarization and the atomic structure at the 180° domain walls. Moreover, the effect of interface terminations on the orientation of polarization vectors and the formation of 180° domain walls have been established. We believe that the attractive results will provide a promising potential for the sustainable development of the ferroelectric

materials and the applications on electronic industries. There are some suggestions for the future work and listed as following.

The present atomic scale mapping technique on the polarization vectors and lattice parameters can be applied to other ferroelectric materials. Therefore, it can provide a comprehensive understanding about general relationship between ferroelectric polarization and the atomic structure at other types of ferroelectric domains and domain walls.

In addition, as the formation of ferroelectric domain walls and the polarization configuration of the domains depend on the interface terminations, the effect of interface terminations on different ferroelectric materials can be further studied to discover the effect of interfacial atomic termination on the mechanism of domains formation. It can also been used to obtain desirable artificial domain structures by the interface termination engineering. This could contribute to the application of ferroelectric materials on future electronic devices.

Moreover, owing to the difference in electrical properties between the ferroelectric domain walls and the bulk domains, it is crucial to explore the underlying reason of difference in electrical properties at domain walls. Therefore,

the desirable domain structures with enhanced electrical properties can be obtained through the interface termination engineering.

References

1. T. Ishihara, Perovskite Oxide for Solid Oxide Furl Cells, Cleveland: Springer, 2009.
2. Z. Haimei , Z. Qian, Z. Florin, S. Matt, S. Florian, C. P. Maria, C. Q. Long, D. Uli and R. R, "Controlling Self- Assembled Perovskite Spinel Nanostructures," Nanoletters, vol. 6, no. 7, pp. 1401-1407, 2006.
3. L. Zhen, Y. Mengjin, P. S. Ji, W. H. Su, B. J. Joseph and Z. Kai, "Stabilizing Perovskite Structures by Tuning Tolerance factor: Formation of formamidinium and Cesium Lead Iodide Solid-State Alloys," Chemistry of Materials, vol. 28, pp. 284-292, 18, Dec 2015.
4. N. Xu, H. Zhao, X. Zhou, W. Wei, X. Lu, W. Ding and F. Li, "Dependence of critical radius of the cubic perovskite ABO3 oxides on the radius of A- and B-site cations," International journal of hydrogen energy, vol. 35, pp. 7295-7301, 25 April 2010.
5. A. K. Prathan, K. Zhang, D. Hunter, J. B. Dadson, G. Loiutts, P. Bhattacharya, R. Katiyar, J. Zhang, D. J. Sellmyer, U. N. Roy, Y. Chi and A. Burger , "Magnetic and electrcial properties of single-phase multiferroic BiFeO3," Journal of Applied Physics, vol. 97, pp. 093903, 1-4, 18 Apr 2005.
6. W. Eerenstein , N. D. Mathur and J. Scott, "Multiferroic and magnetoelectric materials," nature, vol. 442, pp. 759-765, Aug 2006.

7. G. Kieslich, S. Sun and A. K. Cheetham, "An extended tolerance factor approach for organic - inorganic perovskites," Royal society of chemistry, vol. 6, pp. 3430-3433, 14th April 2015.
8. Y.-H. Lee, J. M. Wu and C. H. Lai , "Influence of La doping in multiferroic properties of BiFeO3 thin film," Applied Physics Letters, vol. 88, pp. 42903,1-3, 25 Jan 2006.
9. L. M. Rodriguez-Martinez and J. Paul Attfield, "Cation disorder and size effects in magnetoresistive manganese oxide perovskites," Physical Review B, vol. 54, pp. 622-625, 19 Sep 1996.
10. D. Alikin, A. Turygin, A. Kholkin and V. Shur, "Ferroelectric domain structure and local piezoelectric properties of lead-free (Ka0.5Na0.5)NbO3 and BiFeO3-based piezoelectric ceramics," Materials, vol. 10, no. 1, pp. 1-23, 7 Jan 2017.
11. R. J. H. Voorhoeve, D. W. Johnson Jt., J. O. Remeika and P. K. Gallagher, "Perovskite oxides: materials science in catalysis," Science, vol. 195, no. 4281, pp. 827-833, 04 Mar 1977.
12. Y. Xu, ferroelectric materials and their applications, The Netherlands: Elsevier Science Publishers, 1991.
13. M. E. Lines and A. M. Glass, Principles and applications of ferroelectrics and related materials, New York: Oxford University Press, 2001.
14. Y. L. Tang, Y. L. Zhu, Y. J. Wang, W. Y. Wang, Y. B. Xu, W. J. Ren, Z. D. Zhang and X. L. Ma, "Atomic-scale mapping of dipole frustration at 90 charged domain walls in ferroelectric PbTiO3 films," Scienticfic reports, vol. 4, no. 4115, pp. 1-9, 18 Feb 2014.

15. Y. Liu, Y. L. Zhu, Y. L. Tang and X. L. Ma, "An effect of crystal tilt on the determination of ions displacements in perovskite oxides under BF/HAADF-STEM imaging mode," Jornal of materials research, vol. 32, no. 5, pp. 947-956, 10 Oct 2016.
16. W. Y. Wang, Y. l. Tang, Y. L. Zhu, Y. B. Xu, Y. Liu, Y. J. Wang , S. Jagadeesh and X. L. Ma, "Atomic level 1D structural modulations at the negatively charged domain walls in BiFeO3 films," Advacned materials interfaces, vol. 2, pp. 1500024, 1-9, 30 April 2015.
17. H. H. Huang, Z. Hong, H. L. Xin, D. Su, L. Q. Chen, G. Huang, P. R. Munroe and N. Valanoor, "Nanoscale origins of ferroelastic domain wall mobility in ferroelectric multilayers," Acsnano, vol. 10, no. 11, pp. 10126-10134, 31 Oct 2016.
18. C. L. Jai, V. Nagarajan, J. Q. He, L. Houben, T. Zhao, R. Ramesh, K. Urban and R. Waser, "Unit cell scale mapping of ferroelectricity and tetragonality in epitaxial ultranthin ferroelectric films," Nature materials, vol. 6, pp. 64-69, 17 Dec 2006.
19. Y. Wang, C. Nelson, A. Melville, B. Winchester, S. Shang, Z. K. Liu, D. G. Schlom, X. Pan and L. Q. Chen, "BiFeO3 Domain wall energies and structures: A combined experimental and density functional theory + U study," Physical review letters, vol. 110, pp. 267601, 1-5, 28 Jun 2013.
20. N. A. Hill, "Why are there so few magnetic ferroelectrics?," The journal of physical chemistry B, vol. 104, no. 29, pp. 6694-6709, 3 Jun 2000.

21. T. Hotta, S. Yunoki, M. Mayr and E. Dagotto, "A type Antiferromagnetic and C type Orbital ordered state in LaMno3 using cooperative jahn teller phonons," Physical review B, vol. 60, pp. 1-4, 1 Dec 1999.
22. Y. Zong, K. Fujita, H. Akamatsu, S. Murai and K. Tanaka, "Antiferromagnetism of perovskite EuZrO3," Journal of solid state chemistry, vol. 183, pp. 168-172, 29 Oct 2009.
23. L. Inovecky, "Rotation of domain states in ferroelastic domain structures," Acta Physica Polonica A, vol. 93, pp. 1-11, 1998.
24. W. Pompe, X. Gong, Z. Suo and J. S. Speck, "Elastic energy release due to domain formation in the strained epitaxy of ferroelectric and ferroelastic films," Journal of Applied physics, vol. 74, no. 10, pp. 6012-6019, 15 Nov 1993.
25. S. K. Streiffer, C. B. Parker, A. E. Romanov, M. J. Lefevre, L. Zhao, J. S. Speck, W. Pompe, C. M. Foster and G. R. Bai, "Domain patterns in epitaxial rhombohedra; ferroelectric films. I. Geometry and experiments," Journal of applied physics, vol. 83, no. 5, pp. 2742-2753, 1 Mar 1998.
26. S. W. Cheong, D. Talbayev, V. Kiryukhin and A. Saxena, "Broken symmetries, non-reciprocity, and multiferroicity," npj Quantum materials, vol. 3, no. 19, pp. 1-5, 28 Feb 2018.
27. G. Lawes and G. Srinivasan, "Introduction to magnetoelectric coupling and multiferroic films," Journal of Physics D, vol. 44, p. 243001, 1 Apr 2011.
28. Y. Wang and G. J. Weng, "Magnetoelectric coupling and overall properties of multiferroic composites with 0-0 and 1-1 connectivity," Journal of applied physics , vol. 118, pp. 174102, 1-13, 3 Nov 2015.

29. M. Daraktchiev, G. Catalan and J. F. Scott, "Landau theory of domain wall magnetoelectricity," Physical review B, vol. 81, pp. 224118, 1-12, 30 Jun 2010.

30. C. A. F. Vaz, J. Hoffman, C. H. Ahn and R. Ramesh, "Magnetoelectric Coupling effects in multiferroic complex oxide composite structures," Advanced materials, vol. 22, pp. 2900-2918, 2010.

31. C. W. Huang, Z. H. Chen , J. Wang , T. Sritharan and L. Chen , "Stability and crossover of 71 and 109 domains influenced by the film thickness and depolaization field in rhombohedral ferroelectric thin films," Journal of applied physics, vol. 110, pp. 014110, 1-5, 14 Jul 2011.

32. A. Crassous, T. Sluka, C. S. Sandu and N. Setter , "Thickness dependence of domain wall patterns in BiFeO3 thin films," ferroelectrics, vol. 480, no. 1, pp. 41-48, 6 Jul 2015.

33. J. Liu, W. Chen, B. Wang and Y. Zheng, "Theoretical methods of domain structures in ultrathin ferroelectric films: A review," Materials, vol. 7, pp. 6502-6568, 18 Aug 2014.

34. Y. L. Li, S. Y. Hu, Z. K. Liu and L. Q. Chen, "Effect of electrical boundary conditions on ferroelectric domain structures in thin films," Applied physicsletters, vol. 81, pp. 427-429, 14 May 2002.

35. C. T. Nelson, B. Winchester, Y. Zhang, S. J. Kim, A. Melville, C. Adamo, C. M. Folkman, S. H. Baek, C. B. Eom, D. G. Schlom, L. Q. Chen and X. Pan, "Spontaneous vortex nanodomain arrays at ferroelectric heterointerfaces," Nanoletters, vol. 11, p. 8280834, 19 Jan 2011.

36. D. Lee, R. K. Behera, P. Wu, H. Xu, Y. L. Li, S. B. Sinnott, S. R. Phillpot, L. Q. Chen and V. Gopalan, "Mixed Bloch Neel Ising character of 180 ferroelectric domain walls," Physical review B, vol. 80, pp. 060102, 1-4, 9 Oct 2009.

37. P. Marton , I. Rychetsky and J. Hlinka, "Domain walls of ferroelectric BaTiO3 within the Ginzburg-Landau-Devonshire phenomenological model," Physical review B, vol. 81, pp. 1-12, 11 Jan 2010.

38. V. Zelezny, D. Chvostova, L. Pajasova and I. Vrejoiu, "Optical properties of epitaxial BiFeO3 thin films," Applied Physics A, vol. 100, pp. 1217-1220, 1 Jul 2010.

39. G. Zhang, H. Wu, G. Li, Q. Huang, C. Yang, F. Huang, F. Liao and J. Lin, "New high Tc multiferroics KBiFe2O5 with narrow band gap and promising photovoltaic effect," Scientific Reports, vol. 3, no. 1265, pp. 1-8, 12 Feb 2013.

40. F. Kubel and H. Schmid, "Structure of a ferroelectric and ferroelastic monodomain crystal of the perovskite BiFeO3," Acta crystallographica section B, vol. 46, pp. 698-702, 1990.

41. A. M. Glazer, "The classification of tilted octahedra in perovskites," Acta crystallographica section B, vol. 28, pp. 3384-3392, 1972.

42. J. Seidel, L. W. Martin, Q. He, Q. Zhan, Y. H. Chu, A. Rother, M. E. Hawkridge, P. Maksymovych, P. Yu, M. Gajek, N. Balke, S. V. Kalinin, S. Gemming, F. Wang, G. Catalan, J. F. Scott, N. A. Spaldin, J. Orenstein and R. Ramesh, "Conduction at domain walls in oxide multiferroics," Nature materials, vol. 8, pp. 229-234, 25 Jan 2009.

43. S. Farokhipoor and B. Noheda, "Conduction through 71 domian walls in BiFeO3 thin films," Physical review letters, vol. 107, pp. 127601, 1-4, 16 Sep 2011.

44. T. Choi, Y. Horibe, H. T. Yi, Y. J. Choi , W. Wu and S. W. Cheong, "Insulating interlocked ferroelectric and structural antiphase domain walls in multiferroic YMnO3," Nature materials, vol. 9, pp. 253-258, 14 Feb 2010.

45. M. M. Yang, A. Bhatnagar, Z. D. Luo and M. Alexe, "Enhancement of local photovoltaic current at ferroelectric domain walls in BiFeO3," Scientific reports, vol. 7, no. 43070, pp. 1-8, 20 Feb 2017.

46. L. Li, P. Gao, C. T. Nelson, J. R. Jokisaari, Y. Zhang, S. J. Kim, A. Melville, C. Adamo, D. G. Schlom and X. Pan, "Atomic scale structure changes induced by charged domain walls in ferroelectric materials," nanoletters, vol. 13, no. 11, pp. 5218-5223, 26 Sep 2013.

47. C. M. Fancher, S. Brewer, C. C. Chung, S. Rohrig, T. Rojac, G. Esteves, M. Deluca, N. B. Gharb and J. L. Jones, "The contribution of 180 domain wall motion to dielectric properties quantified in situ X-ray diffraction," Acta Materialia, vol. 126, pp. 36-43, 27 Dec 2016.

48. C. W. Bark, D. A. Felker, Y. Wang, Y. Zhang, H. W. Jang, C. M. Folkman, J. W. Park, S. H. Baek, H. Zhou, D. D. Fong, X. Q. Pan, E. Y. Tsymbal, M. S. Rzchowski and C. B. Eom, "Tailoring a two dimensional electron gas at the LaAlO3/SrTiO3 (001) interface by epitaxial strain," PNAS, vol. 108, no. 12, pp. 4720-4724, 22 Mar 2011.

49. L. W. Martin, Y. H. Chu and R. Ramesh, "Advances in the growth and characterization of magnetic, ferroelectric, and multiferroic oxide thin films," Materials science and engineering R, vol. 68, pp. 89-133, 21 April 2010.

50. J. Wang, J. B. Neaton, H. Zheng, V. Nagarajan, S. B. Ogale, B. Liu, D. Viehland, V. Vaithyanathan, D. G. Schlom, U. V. Waghmare, N. A. Spaldin, K. M. Rabe, M. Wuttig and R. Ramesh, "Epitaxial BiFeO3 multiferroic thin film heterostructures," Science, vol. 299, no. 5613, pp. 1719-1722, 14 Mar 2003.

51. D. G. Schlom, L. Q. Chen , X. Pan, A. Schmehl and M. A. Zurbuchen, "A thin film approach to engineering functionality into oxides," Journal of the american ceramic society , vol. 91, no. 8, pp. 2429-2454, 2008.

52. D. G. Schlom, L. Q. Chen, C. B. Eom, K. M. Rabe, S. K. Streiffer and J. M. Triscone, "Strain tuning of ferroelectric thin films," Annual review of materials research, vol. 37, pp. 589-626, 7 May 2007.

53. R. Eason, Pulsed laser deposition of thin films, United States of America: John Wiley & Sons, Inc.,Publication, 2007.

54. I. M. Dildar, M. Neklyudova, Q. Xu, H. W. Zandbergen, S. Harkema, D. Boltje and J. Aarts, "Growing LaAlO3/SrTiO33 interface by sputter deposition," American Institute of Physics, vol. 5, no. 6, 2015.

55. F. Johann, A. Morelli, D. Biggemann, M. Arredondo and I. Vrejoiu, "Epitaxial strain and electric boundary condition effects on the structural and ferroelectric properties of BiFeO3 films," Physical review B, vol. 84, pp. 094195, 1-10, 19 Sep 2011.

56. H. W. Jang, D. Ortiz , S. H. Baek, C. M. Folkman, R. R. Das, P. Shafer, Y. Chen, C. Nelson, X. Pan, R. Ramesh and C. B. Eom, "Domain engineering for enhanced ferroelectric properties of epitaxial (001) BiFeO3 thin films," Advanced materials , vol. 21, pp. 817-823, 22 Jan 2009.

57. Y. H. Chu, Q. He, C. H. Yang, P. Yu, L. W. Martin, P. Shafer and R. Ramesh, "Nanoscale control of domain architectures in BiFeO3 thin films," Nanoletters, vol. 9, no. 4, pp. 1726-1730, 8 Mar 2009.

58. S. Geller and E. A. Wood, "Crystallograhic studies of perovskite like compounds. I. Rare earth orthoferrites and YFeO3, YCrO3, YAlO3," Acta crystallographica, vol. 9, pp. 563-568, 1956.

59. Y. H. Chu, T. Zhao, M. P. Cruz, Q. Zhan, P. L. Yang, L. W. Martin, M. Huijben, C. H. Yang, F. Zavaliche, H. Zheng and R. Ramesh, "Ferroelectric size effects in multiferroic BiFeO3 thin films," Applied physics letters, vol. 90, pp. 252906, 1-3, 20 Jun 2007.

60. F. Zavaliche, S. Y. Yang, T. Zhao, Y. H. Chu, M. P. Cruz, C. B. Eom and R. Ramesh, "Multiferroic BiFeO3 films: domain structure and polarization dynamics," Phase transitions, vol. 79, no. 12, pp. 991-1017, 11 Jan 2007.

61. D. Sando , A. Barthelemy and M. Bibes, "BiFeO3 epitaxial thin films and devices: past, present and future," IOP publishing, vol. 26, pp. 473201, 1-23, 29 Oct 2014.

62. H. J. Butt, B. Cappella and M. Happl, "Force measurements with the atomic force microscope: Technique, interpretation and applications," Surface science reports, vol. 59, pp. 1-152, 1 Aug 2005.

63. Y. H. Chu, Q. Zhan and L. W. Martin, "Nanoscale domain control in multiferroic $BiFeO_3$ thin films," Advanced Materials, vol. 18, pp. 2307-2311, 2006.

64. S. V. Lainin, S. Jesse, B. J. Rodriguez, J. Shin, A. P. Baddorf, H. N. Lee, A. Borisevich and S. J. Pennycook, "Spatial resolution, information limit, and contrast transfer in piezoresponse force microscopy," Institute of physics publishing, vol. 17, pp. 3400-3411, 15 Jun 2006.

65. C. D. Wright, M. M. Aziz, P. Shah and L. Wang, "Scanning probe memories-technology and applications," Current applied physics, vol. 11, pp. 104-109, 1 Feb 2011.

66. Z. L. Wang, Elastic and inelastic scattering in electron diffraction and imaging, New York: Springer science+business media, LLC, 1995.

67. A. R. Luipini and S. J. Pennycook, "Localization in elastic and inelastic scattering," Ultramicroscopy, vol. 96, pp. 313-322, 3 Nov 2002.

68. R. F. Egerton, "Control of radiation damage in the TEM," Ultramicroscopy, vol. 127, pp. 100-108, 25 Jul 2012.

69. L. Reimer, R. Rennekamp, I. Fromm and M. Langenfeld, "Contrast in the electron spectroscopic imaging mode of a TEM," Journal of microscopy, vol. 162, no. 1, pp. 3-14, Apr 1991.

70. C. L. Jia, M. Lentzen and K. Urban, "Atomic resolution imaging of oxygen in pervoskite ceramics," Science, vol. 299, no. 5608, pp. 870-873, 07 Feb 2003.

71. A. Thust, M. H. F. Overwijk, W. M. J. Coene and M. Lentzen, "Numerical correction of lens aberration in phase retrieval HRTEM," Ultramicroscopy, vol. 64, pp. 249-264, 8 Jan 1996.

72. S. J. L. Billinge and I. Levin, "The problem with determining atomic structure at the nanoscale," Science , vol. 316, no. 5824, pp. 561-565, 27 Apr 2007.

73. O. L. Krivanek, M. F. Chisholm, V. Nicolosi, T. J. Pennycook, G. J. Corbin, N. Dellby, M. F. Murfitt, C. S. Own, Z. S. Szilagyi, M. P. Oxley, S. T. Pantelides and S. J. Pennycook, "Atom by atom structural and chemical analysis by annular dark field electron microscopy," nature, vol. 464, pp. 571-574, 25 Mar 2010.

74. E. Okunishi, I. Ishikawa, H. Sawada, F. Hosokawa and M. Hori, "Visualization of light elements at ultrahigh resolution by STEM annular bright field microscopy," microscopy society of america , vol. 15, p. 164, 2009.

75. S. D. Findlay, N. Shibata, H. Sawada, E. Okunishi, Y. Kondo and Y. Ikuhara, "Dynamics of annular bright field imaging in scanning transmission electron microscopy," ultramicroscopy , vol. 110, pp. 903-923, 13 Apr 2010.

76. A. M. Glazer and S. A. Mabud, "Powder profile refinement of lead zirconate titanate at several temperature. II. Pure PbTiO3," Acta Cryst., vol. 34, pp. 1065-1070, 1978.

77. S. C. Abrahams, S. K. Kurtz and P. B. Jamieson, "Atomic displacement relationship to Curie temperature and spontaneous polarization in displacive ferroelectrics," Physical review , vol. 172, no. 2, pp. 551-553, 28 Feb 1968.

78. J. Seidel, O. Maksymovych, and Y. Batra, "Domain wall conductivity in La-doped $BiFeO_3$," Physical review letters, vol. 105, pp. 1-3, 5 Nov 2010.

79. J. Seidel, G. S. Bhalla and Q. He, "Domain wall functionality in $BiFeO_3$," Phase transitions , vol. 86, no. 1, pp. 53-66, 21 Jun 2012.

80. Q. He, C. H. Yeh, and J. C. Yang, "Magnetotransport at domain walls in $BiFeO_3$," Physical review letters, vol. 108, pp. 1-5, 10 Feb 2012.

81. W. Y. Wang , Y. L. Zhu, Y. L. Tang and M. J. Han, "Atomic mapping of structural distortions in 109 domain patterned BiFeO3 thin films," Journal of materials research, vol. 32, no. 12, pp. 2423-2430, 28 Jun 2017.

82. P. Kaur, K. K. Sharma, R. Pandit, R. J. Choudhary and R. Kumar, "Structural, electrical, and magnetic properties of SrRuO3 thin films," Applied physics letters, vol. 104, pp. 081608, 1-4, 25 Feb 2014.

83. G. Herranz, B. Martinez and J. Fontcuberta, "Enhanced electron-electron correlations in nanometric SrRuO3 epitaxial films," Physical review B, vol. 67, pp. 174423, 1-8, 29 May 2003.

84. P. Wurfel and I. P. Batra, "Depolarization field induced instability in thin ferroelectric films-experiment and theory," Physical review B, vol. 8, no. 11, pp. 5126-5133, 1 Dec 1973.

85. R. Landauer, "Electrostatic considerations in BaTiO3 domain formation during polarization reversal," Journal of applied physics, vol. 28, no. 2, pp. 227-234, 27 Aug 1956.

86. Y. C. Chen, C. H. Ko, Y. C. Huang, J. C. Yang and Y. H. Chu, "Domain relaxation dynamics in epitaxial BiFeO3 films: role of surface charges," Journal of applied physics, vol. 112, pp. 052017, 1-6, 4 Sep 2012.

87. Y. H. Chu, M. P. Cruz, C. H. Yang, L. W. Martin, P. L. Yang, J. X. Zhang, K. Lee, P. Yu, L. Q. Chen and R. Ramesh , "Domain control in multiferroic

BiFeO3 through substrate vicinality," Advanced materials , vol. 19, pp. 2662-2666, 2007.

88. J. E. Giencke, C. M. Folkman, S. H. Baek and C. B. Eom, "Tailoring the domain structure of epitaxial BiFeO3 thin films," Current opinion in solid state and materials science, vol. 18, pp. 39-45, 22 Nov 2013.
89. C. J. M. Daumont, S. Farokhipoor, A. Ferri, J. C. Wojdel, J. Iniguez, B. J. Kooi and B. Noheda, "Tuning the atomic and domain structure of epitaxial films of multiferroic BiFeO3," Physical review B, vol. 81, pp. 1-5, 15 Apr 2010.
90. Z. H. Chen, A. R. Damodaran , R. Xu, S. Lee and L. W. Martin, "Effect of "Symmetry mismatch" on the domain structure of rhombohedral BiFeO3 thin films," Applied physics letters, vol. 104, pp. 182908, 1-4, 8 May 2014.
91. X. Liu, Y. Wang, J. D. Burton and E. Y. Tsymbal, "Polarization controlled ohmic to schottky transition at a metal/ferroelectric interface," Physical review B, vol. 88, pp. 165139, 1-6, 30 Oct 2013.
92. F. Chen and A. Klein, "Polarization dependence of schottky barrier heights at interfaces of ferroelectrics determined by photoelectron spectroscopy," Physical review B, vol. 86, pp. 094105, 1-7, 5 Sep 2012.
93. S. J. Clark and J. Robertson, "Band gap and schottky barrier heights of multiferroic BiFeO3," Applied physics letters, vol. 90, pp. 132903, 1-3, 26 Mar 2007.
94. X. Fang and T. Kobayashi, "Study of pulsed laser deposition of RuO2 and SrRuO3 thin films," Applied physics A, vol. 69, pp. 587-590, 28 Dec 1999.

95. S. M. Sze and K. K. Ng, Physics of semiconductor devices, United State of America: A John wiley & sons, inc, publication, 2007.

96. H. Lu, X. Liu, J. D. Burton, C. W. Bark, Y. Wang, Y. Zhang, D. J. Kim, A. Stamm, P. Lukashev, D. A. Felker, C. M. Folkman, P. Gao, M. S. Rzchowski, X. Q. Pan, C. B. Eom, E. Y. Tsymbal and A. Gruverman, "Enhancement of ferroelectric polarization stability by interface engineering," Advanced materials, vol. 24, pp. 1209-1216, 2012.

97. K. H. Chew, K. G. Lim and L. H. Ong, "Polarization discontinuity and interface charges in ferroelectric superlattices," Ferroelectrics, vol. 490, p. 1490158, 29 Jan 2016.

98. M. Huijen, A. Brinkman, G. Koster , G. Rijnders, H. Hilgenkamp and D. H. A. Blank, "Structure property relation of SrTiO3/LaAlO3 interfaces," Advanced materials, vol. 21, pp. 1665-1677, 2009.

99. F. Pailloux, D. Imhoff, T. Sikora, A. Barthelemy, J. L. Maurice, J. P. Contour, C. Colliex and A. Fert, "Nanoscale analysis of a SrTiO3/La2/3Sr1/3MnO3 interface," Physical review B, vol. 66, pp. 014417, 1-9, 8 Jul 2002.

100. N. Nakagawa, H. Y. Hwang and D. A. Muller, "Why some interfaces cannot be sharp," Nature materials , vol. 5, pp. 204-209, 22 Jan 2006.

101. P. Yu, W. Luo, D. Yi, J. X. Zhang, M. D. Rossell, C. H. Yang, L. You, G. S. Bhalla, S. Y. Yang, Q. He, Q. M. Ramasse, R. Erni, L. W. Martin, Y. H. Chu, S. T. Pantelides, S. J. Penntcook and R. Ramesh, "Interface control of bulk ferroelectric polarization," PNAS, vol. 109, no. 25, pp. 9710-9715, 19 Jun 2012.

102. R. Egoavil, H. Tan, J. Verbeeck, S. Bals, B. Smith, B. Kuiper, G. Rijnders, G. Koster and G. V. Tendeloo, "Atomic scale investigation of a PbTiO3/SrRuO3/DyScO3 heterostructure," Applied physics letters, vol. 102, pp. 223106, 1-5, 5 Jun 2013.

103. H. J. Chang, S. V. Kalinin, A. N. Morozavska, M. Huijen, Y. H. Chu, P. Yu , R. Ramesh, E. A. Eliseev, G. S. Svechnikov, S. J. Pennycook and A. Y. Borisevich, "Atomically resolved mapping of polarization and electric fields across ferroelectric/oxide interfaces by Z-contrast imaging," Advanced materials, vol. 23, pp. 2474-2479, 2011.